A PRELIMINARY DESIGN METHODOLOGY FOR FATIGUE LIFE PREDICTION OF POLYMER COMPOSITES FOR TIDAL TURBINE BLADES

Ciaran R. Kennedy, Sean B. Leen, Conchúr M. Ó Brádaigh
Mechanical and Biomedical Engineering, NUI Galway, Ireland

ABSTRACT

Tidal turbine blades experience significant fatigue cycles during operation and it is expected that fatigue strength will be a major consideration in their design. Glass fibre reinforced polymers (GFRP) are a candidate low-cost material for this application. This paper presents a methodology for preliminary fatigue design of GFRP tidal turbine blades. The methodology combines (i) a hydrodynamic model for calculation of local distributions of fluid-blade forces, (ii) a finite element structural model for prediction of blade strain distributions, (iii) a fatigue damage accumulation model, which incorporates mean stress effects, and (iv) uniaxial fatigue testing of two candidate GFRP materials (for illustrative purposes). The methodology is applied here to the preliminary design of a three-bladed tidal turbine concept, including tower shadow effects, and comparative assessment of pitch-regulated and stall-regulated control with respect to fatigue performance.

1. INTRODUCTION

The emerging field of ocean energy is naturally turning to composite materials because of their perceived non-corrosive properties in the harsh saltwater environment as well as their high specific strength and stiffness. Tidal turbines are to the forefront due to their reliable and predictable power delivery to the grid and the absence of overload conditions. A number of different designs of tidal turbines are already at utility scale trials. A low-solidity, two-bladed turbine, similar to wind turbines, and a high solidity, multi-blade, ducted rotor are presently undergoing customer testing [1]. Wave energy converters are also under consideration with a number of devices at full size prototype stage [2]. Glass-fibre reinforced polymers (GFRP) are candidate low-cost materials for the blades of tidal turbines and the energy collection surfaces of wave devices. It is therefore important to understand the durability and performance of such materials for these applications. A 10 rpm tidal turbine would see approximately 4 million revolutions per year and wave devices will encounter approximately the same number of waves. Therefore fatigue failure will need to be considered in the design of these devices.

The structural properties of GFRP materials depend on orientation of the fibres, polymer type and fibre/polymer volume fraction. One of the main advantages of fibre reinforced materials is the ability to align the strong, stiff fibres with the main loads and thereby use the material to its maximum advantage. There are situations, however, particularly in relation to emerging technologies e.g. ocean energy, where (i) the loads are not very well understood, or (ii) the loads are complex and multi-directional in nature, for which a class of fibre-reinforced laminates called quasi-isotropic (QI) can be used. The typical QI layup has equal numbers of fibres at 0, 45, 90, and 135 degrees although many other configurations are possible. Often QI laminates are used for an entire structure or they can be implemented locally on other laminate types by adding extra plies of reinforcement around high stress features (e.g. holes). As suggested by the name, QI laminates can be considered to be isotropic for all in-plane properties (at least for 1st order approximations). The tensile strength of QI laminates is primarily determined by the volume fraction of glass fibre (V_f) in

the laminate which normally varies between 30 and 70%. The fatigue strength at high stress is also related to the glass fibre strength, but at high cycles (low stress) the polymer matrix properties become more important in determining fatigue life [3].

Fatigue degradation of composites was best described by Talreja in 1981 as having three distinct zones where the mechanisms of failure are very different [4]. Zone 1 corresponding to high stress cycling where the strains are high enough to break the fibres directly and the number of cycles to failure depends on the random accumulation of fibre breaks at any cross-section reducing the strength of the material below the applied stress. In zone 2 the matrix fractures due to the combination of strain level and cyclic loading but crack growth is arrested by the fibres, through a combination of mechanisms. Cracks accumulate and cause some fibre fracture until the damage reduces the material strength below the applied stress at some (random) cross-section and total fracture occurs. In zone 3 the strain is less than that needed to cause matrix cracking and, although there is inevitably some small damage, it does not grow at an appreciable rate and the number of cycles to failure is essentially infinite.

Just as fibre orientation and volume fraction control the static strength of a composite, these are also are the primary determinants of fatigue strength. In fact in many cases fatigue strength is normalised by UTS and it is generally shown that zone 2 starts around 1000, cycles at approximately 80% of UTS, and drops to approx. 25% of UTS at over 1 million cycles [5]. The matrix and size (bond promoter) also have an influence on both the UTS and fatigue strength with some resins being developed specifically for additional fatigue strength [6] thereby changing the UTS to fatigue strength relationship slightly (~ 8%). Service temperature will impact both UTS and fatigue life in equal measure at least to an initial approximation [5]. Unfortunately UTS prediction is not an exact science but approximations are available [7]; static testing is quicker than fatigue testing, and the equipment and skill needed are less sophisticated. Other materials-related influences are the detrimental effects of woven fabrics, tightly-stitched fabrics and high volume fractions (above 40% for dry fabrics, above 60% for prepreg) [8]. Low velocity, high mass impact can damage composite laminates [9] and provide nucleation sites for fatigue damage accumulation.

The next set of influences on fatigue life has to do with the nature of the fatigue load experienced by the material. First of these is the relationship between cyclic amplitude and mean stress. This is usually represented in terms of constant life lines (CLL’s) on a Goodman diagram, across a range of R ratios, where R is the ratio of minimum to maximum stress(or strain) in the cycle to maximum stress. Data from [10] and [8] show a complicated pattern where CLL's change shape as the number of cycles to failure rise. In particular it has been shown that, for high cycle fatigue, compressive mean stress is less detrimental and tensile mean stress is more detrimental than would be expected by the classical triangular Goodman lines. The influence of off-axis loading or normal and shear stresses on fatigue strength has been extensively studied [11] with shear stresses seen to be the more detrimental [12]. Various failure models have been proposed and a review [13] shows that a modified Tsai-Hill criterion is promising. The sequence of load cycles is also shown to be important with random spectrum loading shown to reduce life by over 50% compared to more ordered spectra [14]. This is seen as a key deficit of Miner's summation method but so far no other method explains this phenomena well and work on fatigue damage evolution continues [15][16].

Fatigue testing of coupons using various measurement techniques provides insight into the fatigue behaviour of GFRP. High frequency cyclic loading (>10 Hz) has been shown to cause autogenous heating and early failure [10] so that low frequency testing is necessary. Constant rate of strain application (RSA) testing is recommended and can help speed up testing at high cycles [5]. Waveform (Triangular, Sinusoidal, of Square wave) has been shown

to have some effect at low cycles [17] but little effect at high cycles [5]. All fatigue failures in laminated GFRP are preceded by significant matrix cracking. In fact a characteristic of these materials is that damage spreads throughout a large area of the coupon (at least in straight sided tensile specimens) before becoming localised and causing failure [18]. Matrix cracking always starts in the most off-axis ply and fatigue matrix cracking starts at lower strains than during quasi-static testing [19]. These cracks always start at the edge of the coupon [19] and appear to be significantly suppressed (approximately two decades) in structures with no free edges [17][20]. Matrix cracking causes an initial drop in stiffness followed by a further slow decline over most of the fatigue life finishing with a final sharp drop to failure [21]. Total stiffness loss during this process is of the order of 10 to 20% [22]. Residual strength has a similar pattern [23] and both phenomena have been used to model damage in composite laminates [24]. In fact many models have been proposed for composite fatigue but all require careful application by the analyst. Fatigue testing of actual components under realistic loadings remains the only way to reliably determine the fatigue life of composite materials.

Despite a vast and fascinating variety of proposed configurations for tidal (or marine current) turbines [25] it must be conceded that the standard wind turbine configuration (horizontal axis, upwind, 3 bladed, pitch regulated) will be the benchmark against which all other proposals for tidal turbines are measured. Hydrodynamic design of tidal turbine blades can be expected to follow a similar pattern to that of wind turbine blades. Blade element momentum approaches have already been verified [26] and investigation of cavitation shows that it should not be a problem [27]. Blade element momentum theory is used for preliminary design of wind turbine rotors [28] following a method suggested by Glauert using tip loss factors according to Prandtl. Modelling wake rotation improves the accuracy of BEM and Van Briel has detailed a technique to avoid numerical difficulties near the hub [29]. Detailed design of wind turbine rotors uses specialised aeroelastic codes [30].

This paper develops a methodology for preliminary design of tidal turbine blades based on a minimum number of input parameters to predict the fatigue life of blades. The method is applied to the preliminary investigation of a number of design aspects for tidal turbines.

2. METHOD

The turbine blade fatigue design methodology, as depicted in Figure 1, is modular in nature, consisting of a number of separate models, combined to facilitate the hydrodynamic and structural calculations required for preliminary design of a tidal turbine blade with respect to fatigue life. A central aspect of the present design methodology (and associated testing) is that it is predicated on blade fabrication from a fibre-reinforced polymer composite material although, clearly, the proposed methodology could be readily adapted for alternative materials, e.g. metallic candidate materials. With reference to Figure 1, the first module in the design process model is a tidal model, which predicts the tidal current speed at any time for specified pertinent local tidal velocities (typically measured). The output from this tidal model forms a key input to a hydrodynamic model (based on a streamtube or blade element momentum approach), which in turn computes the radial distributions (for each streamtube) of (i) local relative blade-fluid velocities, (ii) axial and tangential blade forces, (iii) optimum chord length and (iv) pitch angle. The subsequent structural module, based on development of a finite element model of the blade, and driven by the output from the hydrodynamic model, is then employed to characterise the strain distribution (and hence maximum strain) in the turbine blade. The fatigue model accounts for each rotation of the blade explicitly and determines the maximum strain in the blade for each cycle. It then takes that maximum strain (and an assumed cyclic component), compares them to an experimentally determined strain-life curve for the material and obtains a damage fraction for that cycle. Summation of the damage fractions using Miner's rule gives an estimate for the life of the tidal turbine blade.

2.1 Tidal Model

Normally there are two high and two low tides of roughly equal magnitude per day with the magnitude varying by approximately 40% in a repeating monthly cycle. The highest tides, called spring tides, occur when the sun and moon are in alignment. This happens twice in each cycle. The lowest tides, called neap tides, also happen twice per cycle when the moon is at 90° to the sun [1]. Figure 2(a) shows a typical tide height pattern from the west coast of Ireland [31]. Tidal currents become magnified in areas where large bodies of water are connected to the main sea by relatively small inlets. The water speed depends on the local topography, but if the spring and neap maximum velocities are measured, the full cycle can be approximated by a combination of a semi-diurnal sinusoid and a fortnightly sinusoidal function [32] [33]. The tidal current velocity at any time t is

$$V_t = \cos(\omega_d t)\,[v_{ave} + v_{alt}\cos(\omega_m t)] \tag{1}$$

where v_{ave} is the average of the peak tidal velocities, v_{alt} is half the range of peak tidal velocities, ω_d is the angular frequency of the tides, and ω_m is the angular frequency of the spring-neap (14.7 day) cycle. Figure 2b shows the pattern given by Equation 1.

2.2 Hydrodynamic Model

The tidal current flows over the turbine blades creating lift and drag which turn the blades and power the turbine. The lift and drag forces can be estimated to a first order approximation using a stream tube momentum model [34]. The model, as shown in Figure 3, assumes a series of isolated concentric tubes within which momentum loss is in balance with the forces acting on the blade. For steady state operation the fluid forces on the blades inside any stream tube must equal the momentum lost from that stream tube

$$F_A = \left(\frac{2\dot{M}}{N}\right)\left(V_t - U_d(R)\right) \tag{2}$$

where F_A is the sum of the axial components of the lift and drag forces on the blade element inside the tube, N is the number of blades on the turbine and $\dot{M}$ is the mass flow rate through the tube, V_t is the tidal current velocity and U_d is the axial water velocity at the rotor disk. The factor of 2 appears in the equation because, as [28] shows, half the total reduction in velocity occurs upstream of the turbine blades. A similar argument pertains to the relationship between torque and angular momentum of the fluid. Within each stream tube the tangential components of the lift and drag forces sum to give a torque producing force and this imparts angular momentum to the blade. This angular momentum is balanced by an angular momentum of the fluid in the opposite direction, causing wake rotation. Transformation to a rotating coordinate system and making the assumption that the relative resultant water velocities are constant allows generation of equations [29] giving axial and rotational velocity at the disk, as follows:

$$U_d = \frac{V_t}{\pi}\sqrt{1 + \gamma^2 + \zeta - \gamma\sqrt{(1 + \gamma^2 - \zeta^2)}} \tag{3}$$

$$V_d = U_d\,\frac{\sqrt{1 + \gamma^2 - \zeta^2} - \gamma}{1 - \zeta} \tag{4}$$

where U_d is the axial velocity in a stream tube at the rotor disk, V_d is the tangential velocity (swirl) of the fluid in a stream tube at the rotor disk, ζ is the fraction of axial velocity remaining at the downstream exit of the stream tube, and γ is the local blade speed ratio given by

$$\gamma = \frac{\omega_b R}{V_t} \tag{5}$$

where ω_b is the angular velocity of the blade, R is the radius, and V_t is the freestream velocity of the fluid. The blade also has a tangential velocity V_b at the stream tube due to its angular velocity:

$$V_b = \omega_b R \tag{6}$$

The apparent or relative velocity seen by the blade is then (see Figure 3):

$$V_r = \sqrt{{U_d}^2 + (V_d + V_b)^2} \tag{7}$$

and the angle between the relative velocity and the plane of the rotor is given by:

$$\theta = \tan^{-1} \frac{U_d}{V_d + V_b} \tag{8}$$

The lift and drag forces generated by a stream tube on the blade section inside it are thus given by:

$$L = \tfrac{1}{2} C_L {V_r}^2 \rho S \Delta R \tag{9}$$

$$D = \tfrac{1}{2} C_D {V_r}^2 \rho S \Delta R \tag{10}$$

where C_L and C_D are the coefficients of lift and drag for the aerofoil selected, ρ is the density of the fluid, S is the chord length of the blade at the stream tube radius and ΔR is the radial dimension of the stream tube. The lift force is always perpendicular to the fluid velocity and the drag force always parallel. These are translated into axial and tangential forces by

$$F_A = L cos\theta + D sin\theta \tag{11}$$

$$F_C = L sin\theta + D cos\theta \tag{12}$$

where F_A is the axial (thrust) force acting on the blade by that stream tube and F_C is the tangential (torque) force. For maximum power output:

$$U_d = \frac{2}{3} V_t \tag{13}$$

as per the well-known Betz limit. The inputs, outputs, and flowchart of the method of the hydrodynamic program are summarised in Figure 4. The output from the program at each radial increment is: chord length, pitch angle, axial force and tangential force on the blade at that radial increment. The program also predicts the maximum power output, torque and bending moment at the blade root at the chosen water velocity.

Control systems have a significant effect on the forces and moments in a tidal turbine blade, by regulating the power absorbed by the turbine during high water velocity operation. The present hydrodynamic model is used to simulate the two main options for controlling power in tidal turbines, namely pitch-regulation (PR) and stall-regulation (SR). Pitch regulation is a system where the entire blade is rotated about its axis to modify the lift coefficient (C_L) and thereby the forces on the blade. Stall regulated blades have fixed pitch but are designed with a specific radial variation of pitch angle so that as the tidal velocity increases the angle of attack over a portion of the blade exceeds the stall angle and lift drops off reducing the forces on the blade. Wind turbine control systems have evolved to full-span pitch control systems in order to deal with their large operational range of wind velocities (2.5 – 25 m/s). Tidal currents do not exhibit as large a range (typically 0.75 to 3 or 4 m/s) and therefore simpler control systems may be viable for tidal turbines.

2.3 Structural Model

In common with modern wind turbines there is a significant structural challenge in reacting the loads placed on the turbine blades within the slender aerofoil shape of the turbine blade. A set of aerofoil shapes with relatively thick section, 24% of chord length, have been developed e.g. NACA 63-421, RISO-A1-24 (see Figure 5) to achieve good lift and drag performance while maximizing the cross section area moment of inertia allowing for good structural characteristics [35]. The present work is focussed on the fatigue life of a small "low cost" turbine. This low cost version is a 5 m radius, 3-bladed, downstream, free-yaw turbine, which has a theoretical maximum power of 330 kW in a 2.6 m/s tidal current. This configuration eliminates expensive yaw (and possibly pitch) systems and allows for a simple robust construction. A shell element model of the outer 3.5 m of the turbine blade has been constructed in the ABAQUS finite element program as shown in Figure 6. The blade model stops at 1.5 m radius which is the point of maximum chord length predicted by the hydrodynamic model. Inboard of this the blade starts to transition and connect to the steel hub attachment which involves details outside the scope of this study. A short straight section (with a radial dimension of 0.5 m) has been added to the blade to mimic the transition section with particular emphasis on minimizing any stress concentrations at the connection. Details of stress and strain in this transition section are not reported here, since the present work is concerned with the development of a preliminary design capability. All elements in the model are 4-node doubly curved shell elements with reduced integration. A mesh convergence study has been performed and shows that strain results at the mesh density used are essentially converged. The aerofoil shape has been simplified in the structural model, representing the smooth aerofoil curved surface, shown in Figure 5, by a piecewise linear equivalent (Figure 7) but it maintains a section thickness equal to 24% of chord length. Following the practice in the wind turbine industry, e.g. see [36], two shear webs have been inserted into the aerofoil shape creating a box section which becomes the structural core of the blade. The top caps of this box are 35 mm thick near the root (at 1.5 m radius) and taper to 6 mm at the tip. The shear webs and fairings start at 12 mm thick (again at 1.5 m radius) and taper to 4 mm thick at the tip. In the finite element model the panels of the blade are modelled as shell elements with QI material properties from standard laminate analysis [37]. The values chosen here for both epoxy / E-glass and vinyl ester / E-glass are shown in Table 1(a) and 1(b). High stress locations near the surface are modelled with individual plies. Material properties for the individual plies are calculated from the rule of mixtures and the Halpin-Tsai equations [38] as also shown in Table 1(a) and 1(b).

2.4 Experimental Method

Quasi-isotropic laminates have been manufactured here using the VARTM (vacuum assisted resin transfer moulding) process. Biaxial stitched glass-fibre mat (0°-300 g/m^2, 90°-300 g/m^2) was cut to give ±45° material and 0°/90° material and then stacked to create a $[(45\backslash 135\backslash 90\backslash 0)_2]_s$ laminate. Either vinyl ester or epoxy resins were introduced under vacuum to complete the laminate (see Figure 8). After a room temperature cure for 48 hours, the laminates were oven cured at 80° C for 3 to 5 hours. Volume fractions of approximately 50% were achieved at an average thickness of 3.75 mm. The laminates were cut into 25 x 250 mm coupons using a water cooled diamond abrasive disk.

Fatigue tests were performed with an Instron 8500 test machine and 8800 controller applying a sinusoidal force in tension-tension mode (R = 0.1) between 5 and 12 Hz. The frequency is decreased to maintain a constant rate of strain application as the strain level increases [5]. A fan was used to cool the coupon during testing. A radiation thermometer measured less than 10° C temperature rise in surface temperature during the highest stress cycling test. Five coupons were tested at each of four separate stress levels. A power law relationship between maximum initial strain ($\varepsilon_{max,i}$) and fatigue life of the form

$$\varepsilon_{max,i} = AN_f^{-B} \tag{14}$$

where N_f is the number of cycles to failure, and A and B are constants, is found to be a good fit for the data (as shown below).

2.5 Fatigue Model

The fatigue model focuses on the highest tensile strain in the blade, which is predominantly attributed to bending-induced strain. Each cycle of the tide causes a slow increase and then a decrease in the maximum strain on the blade – this is a low-frequency cycle in itself of which there are only two per day. Simultaneously the blade experiences a high frequency cyclic load for each revolution of the machine, caused by the blocking ('shadow') effect of the support tower as shown in Figure 9. The tower causes a reduction in the water velocity downstream of itself and consequently a loss of lift on the blade. Figure 10 shows the drop in bending strain in the blade due to this shadow effect. The magnitude of this brief reduction in bending strain depends on the geometry of the particular turbine. Obviously if the tower blocks the flow completely, the drop in bending moment, and hence strain, approaches 100%. Test data on a downstream wind turbine shows a 30% drop in bending moment [39]. Wave interaction can also lead to fluctuations in the load on tidal turbine blades. Experiments with scaled models of tidal turbines in a wave tank have measured flapwise bending moment amplitudes of 50% [40]. For the present study two cases of 50% and 90% reductions of the bending strains in the tidal turbine blade are considered, corresponding to fatigue loading R-ratios ($\varepsilon_{min}/\varepsilon_{max}$) of 0.5 and 0.1 respectively for the high frequency loading cycle of the combined fatigue cycle shown in Figure 10.

There is no generally accepted method for dealing with the effect of mean stress in fatigue of composites, i.e. for inferring the ε-N curves from one (test) R-ratio to a different R-ratio. The approach adopted here, to infer the R = -1 and R = 0.5 ε-N data from the (measured) R = 0.1 data, is based on that described in [41]. This is based on the following assumed behaviour for constant life diagrams as illustrated in Figure 11:

1. The N_f = 5000 line joins the R = 0.1 test data point to the material ultimate strain, ε_u, data point on the mean strain axis.
2. For -1 ≤ R ≤ 0.5, the CLL's are assumed to be parallel to the N_f = 5000 line, based on experimental observations, e.g. [42].
3. For the R > 0.5, the CLL's join the R = 0.5 data points to the ε_u data point on the mean strain axis.

As the material in the turbine blade is essentially linearly elastic the major strains in the blade are directly proportional to the flapwise bending moment. Therefore the maximum strain at any time *j* is found from the following equation:

$$\varepsilon_{max,j} = \varepsilon_{ref}\left(\frac{M_{\mathrm{f}}(v_j)}{M_{ref}}\right) \tag{15}$$

where $M_{\mathrm{f}}(v_j)$ represents the functional dependence of bending moment on tidal current velocity, M_{ref} is the reference bending moment and ε_{ref} is the maximum strain in the blade when the reference moment is applied.

The fatigue damage calculation involves contributions from two types of load (strain) cycles. The first sums the damage due to the strain cycles caused by the low frequency semi-diurnal tidal cycle (which implicitly includes the lower frequency 14-day tidal cycle effect), while the second sums the damage caused by the higher frequency cycles, due to the tower shadow effect. The fatigue model finds the tidal velocity from Equation 1 and uses Equation 15 to find the maximum strain in the blade during that revolution. Equation 14, with the identified strain-life fatigue constants, then provides the number of cycles to failure at that strain level. For a particular integration point (hot spot) in the FE model of the blade, the damage fractions are then summed to find the 7-day damage and hence the turbine life, using a Miner's rule approach, as follows:

$$D_{7-day} = \sum_{k,tide}^{N_k} \frac{1}{N_{f,k}} + \sum_{j,rev}^{N_j} \frac{1}{N_{f,j}} \tag{16}$$

where N_k is the number of tidal cycles during the 7 day period, N_j is the number of turbine revolutions during the 7 day period, $N_{\mathrm{f,k}}$ and $N_{\mathrm{f,j}}$ are the numbers of cycles to failure for a given combination of mean and alternating strain during each tide and revolution, respectively; *k* is the increment of tidal cycles, and *j* is the increment of revolutions of the turbine. The blade life in years is then given by

$$Blade\ Life_{yrs} = \frac{7.38}{365.25\ D_{7-day}} \tag{17}$$

where 7.38 is the exact length of the 7-day period used (1/4 of a synodic month) and 365.25 is the length of a year in days.

3. RESULTS

Figure 12 shows the strain-life fatigue test results for the epoxy/E-glass and vinyl ester/E-glass materials along with the corresponding power law curve fits, as per Equation 14. The identified fatigue strain-life power-law constants for the two materials are given in Table 2, along with the inferred R = 0.5 constants, based on the mean stress diagram procedure described above. The superior performance of the epoxy resin over the vinyl ester resin is obvious. It is observed during the testing that epoxy appears more tolerant of the cracks and minor delaminations that appear at the edges of the coupon during testing. Certainly the epoxy specimens are more obviously damaged before final failure as can be seen in Figure 13.

Figure 14 shows the predicted radial distribution of blade chord length and pitch angle as determined by the hydrodynamic model for the base case set of parameters described in

Table 3. The blade chord length is 750 mm at the tip, with a pitch angle of 4 degrees. It tapers and twists to a chord length of 1250 mm and a pitch angle of 20 degrees at 1.5 m radius. Figure 15 shows the radial distributions of tangential and thrust forces versus radius as predicted by the same hydrodynamic model, via Equations 11 and 12. The thrust force, which increases linearly with increasing radius from about 0.7 kN to about 2.3 kN at the extreme blade radius, is significantly larger than the (power-generating) tangential force, which increases asymptotically with radius from about 320 N at a small radius to a value of about 410 N at the extreme blade radius. These forces cause a flapwise bending moment of 150 kNm and an edgewise bending moment of 35.7 kNm at 1.5 m radius from the rotor centre. The model uses 45 streamtubes, uniformly distributed along the blade, and assumes that the water in each of these tubes has slowed to 1/3 its initial velocity at the exit of the streamtube (i.e. $\zeta = 0.333$).

Figure 16 shows the deflected shape of the blade when these forces are doubled (to account for a factor of safety of 2) and applied to the FE model described above. The forces are applied as surface traction distributions (in the relevant directions) on the spar caps of the blade. This is based on the assumption that the resultant forces act through the ¼ chord point (¼ of the chord length back from the leading edge of the aerofoil) of each blade section [43]. The tip deflects axially by 334 mm under these loads, which is approximately twice the blade aerofoil thickness at the tip. This amount of deflection will not introduce any significant error into either the structural or hydrodynamic calculations.

The highest stresses and strains are predicted to occur near the hub, in the caps of the box section spar which form the main structural member of the blade. These are primarily caused by the large (flapwise) bending moments due to the thrust force. Bending strains are at their maximum on the outer surface and the maximum principal strains are essentially aligned with blade axis, however it is necessary to find the maximum strains in the fibres to make a legitimate comparison to the experimental fatigue life data. The fibres in the three outermost plies are at 45°, 135° and 90° to the blade axis (and thereby to the maximum principal strain) which reduces their fibre strains. The 4^{th} ply from the surface has its fibres at 0° to the blade axis and therefore aligned with the direction of the principal bending strains. The maximum fibre strains are predicted in this ply, as shown in Figure 17.

The base case results described above have given the maximum fibre strain in the turbine blade at a single (2.6 m/s) water velocity. Equation 15 can then be used to compute maximum fibre strain at any water velocity given the flapwise bending moment at that water velocity. Figure 18 shows the predicted dependence of bending moment near the root of the blade on water velocity, due to thrust forces calculated by the hydrodynamic model, for (i) a PR tidal turbine, (ii) an SR turbine and (iii) an unregulated turbine. Note that the base case discussed above is in the water velocity regime where all three control systems produce the same flapwise moment. Using the hydrodynamic model to predict maximum theoretical power levels for both PR and SR turbines, and integrating over the tidal pattern chosen for this study (i.e. see Figure 2) will give the energy produced by each turbines per year. In order to facilitate an objective comparison of the PR and SR turbines, with respect to fatigue damage accumulation, the energy output from the PR turbine is matched to that of the SR turbine. This is achieved by identifying the threshold value of water velocity for pitch control, above which blade pitch is controlled to give constant flapwise moment (and hence power). The threshold water velocity value of 3.05 m/s (see Figure 18) has been identified here, using the hydrodynamic model described above, for the PR turbine.

In order to predict fatigue damage accumulation, using Equations 14 to 16, the moment-velocity relationships of Figure 18 are fitted with polynomial expressions, to allow interpolation with respect to water velocity. The fatigue reference case, described in Table 4, is analysed by the fatigue model and a fatigue life of 11.6 years is predicted for this case. By

varying each of the parameters in Table 4 the fatigue model will give insight into the effects of each of these on the fatigue life. Figure 19 shows the effects of a strain concentration at the point of maximum strain in the blade. This strain concentration could be as a result of a non uniformity in laminate thickness, a reduction in number of plies or geometric discontinuities, such as bolt holes. The figure predicts that small increases in maximum strain (stress) have a large influence on blade life, with a strain concentration factor SNCF of only 1.1 decreasing fatigue life by 50%, for example.

The fatigue model is also used here to compare the blade life of an SR turbine with that of a PR turbine. The fatigue damage fraction for each rotation of the turbine is sorted into bins based on water velocity (0.1 m/s increments) and Figure 20 shows accumulated damage in each water velocity bin for both the PR and SR blades (note that the area under each curve, which represents total accumulated damage over blade lifetime, is equal to 1.0). The graph shows that the SR blade sustains a lot of damage at high water velocities, due to the higher bending strains, whereas for the PR blade, the damage at high velocities is significantly lower, due to the lower bending strains. Most of the PR blade damage is sustained at medium water velocities, due to the greater number of operational hours in this regime. The fatigue model predicts that a blade which survives 20 years on the PR machine will only survive 12.8 years on the SR machine.

Figure 21 shows some sample predictions based on different design scenarios for the turbine blades, based on the methodology developed here, relative to the predictions for the reference case of Table 4:

- As discussed above a SR turbine blade will have a shorter life than an equivalent PR turbine blade. However the pitch regulation system is expensive and it may be less expensive to oversize the turbine components to deal with the higher loads imposed by a stall regulated control system. The fatigue model predicts that if the laminate thickness in the spar cap of the SR blade is increased by just 10% (which decreases maximum strain by ~5%) it will then have a fatigue life equal to a PR blade (of equal energy generation).
- Vinylester / E-glass has a number of advantages over the Epoxy / E-glass material used in the reference case. These include lower cost and increased resistance to water penetration. However vinylester matrix composites have lower fatigue performance than their epoxy matrix competitors. Using the experimental fatigue data for both of these materials (see Figure 12 and Table 2) in the fatigue model, and integrating with respect to time history of tidal velocity, it is predicted that the maximum strain in a vinyl ester blade must be 29% less than in an epoxy blade, to achieve the same fatigue life.
- The fatigue model has also been used to investigate the effect of increasing tower shadow effect. This could be caused by design changes such as moving the blade closer to the tower or increasing the tower diameter. It is predicted that that increasing tower shadow effect from 50 to 90% requires a reduction of 15% in the maximum blade strain to maintain the same fatigue life.

4. CONCLUSION

This study presents a methodology for preliminary fatigue design of GFRP tidal turbine blades. Uniaxial fatigue testing of two candidate (quasi-isotropic) GFRP materials is carried out to facilitate application of the design methodology to the design of a three-bladed tidal turbine concept for a range of tidal velocities. Some key conclusions from this study are as follows:

- The epoxy/E-glass material is significantly more fatigue resistant than the vinyl ester/E-glass material.

- However, due to the low measured slopes of the strain-life curves for both materials, it is shown that the blade fatigue life is highly sensitive to maximum blade stress and strain level. For example, a 15 % increase in stress is predicted to reduce blade life from 20 years to about 5 years.
- Mean stress effects are shown to be important in the design of a three-bladed concept with respect to tower shadow effect. Specifically, with increasing tower shadow effect from 50% to 90% (in terms instantaneous reduction in blade strain during blade rotation past tower), the reduction in blade fatigue strength (maximum allowable strain) is predicted to be about 15%.
- The fatigue performance of an epoxy/E-glass tidal turbine blade, for the three-bladed concept, with pitch-regulation and including a 50% tower shadow effect, is shown to be approximately 30% better than that of a vinylester/E-glass blade, in terms of maximum allowable strain for a given fatigue life.
- It is shown that blades on a stall regulated tidal turbine need approximately 10% thicker laminates than those on a pitch regulated turbine for a given design fatigue life.

5. ACKNOWLEDGEMENTS

The author wishes to thank ÉireComposites Teo. for manufacture of the laminate specimens, and CTL Tástáil Teo. for preparation of the tensile coupons.

REFERENCES

[1] F. O Rourke, F. Boyle, and A. Reynolds, 'Tidal energy update 2009', *Applied Energy*, vol. 87, no. 2, pp. 398–409, Feb. 2010.

[2] B. Drew, A. R. Plummer, and M. N. Sahinkaya, 'A review of wave energy converter technology', *Proceedings of the Institution of Mechanical Engineers, Part A: Journal of Power and Energy*, vol. 223, no. 8, pp. 887 –902, Dec. 2009.

[3] R. Talreja, 'Damage and fatigue in composites - A personal account', *Composites Science and Technology*, vol. 68, no. 13, pp. 2585–2591, Oct. 2008.

[4] R. Talreja, 'Fatigue of Composite Materials: Damage Mechanisms and Fatigue-Life Diagrams', *Proceedings of the Royal Society of London. A. Mathematical and Physical Sciences*, vol. 378, no. 1775, pp. 461 –475, Nov. 1981.

[5] G. D. Sims, 'Fatigue test methods, problems and standards', in *Fatigue in composites: science and technology of the fatigue response of fibre-reinforced plastics*, Woodhead Publishing, 2003.

[6] C. M. Manjunatha, A. C. Taylor, A. J. Kinloch, and S. Sprenger, 'The Tensile Fatigue Behavior of a GFRP Composite with Rubber Particle Modified Epoxy Matrix', *Journal of Reinforced Plastics and Composites*, vol. 29, no. 14, pp. 2170 –2183, Jul. 2010.

[7] L. J. Hart-Smith, 'Expanding the capabilities of the Ten-Percent Rule for predicting the strength of fibre-polymer composites', *Composites Science and Technology*, vol. 62, no. 12–13, pp. 1515–1544.

[8] J. F. Mandell, D. . Samborsky, N. K. Wahl, and H. J. Sutherland, 'Testing and Analysis of Low Cost Composite Materials Under Spectrum Loading and High Cycle Fatigue Conditions', in *Proceedings of The 14th International Conference on Composite Materials (ICCM-14)*, Society of Manufacturing Engineers, 2003, p. Paper 1811.

[9] P. . Bland and J. . Dear, 'Observations on the impact behaviour of carbon-fibre reinforced polymers for the qualitative validation of models', *Composites Part A: Applied Science and Manufacturing*, vol. 32, no. 9, pp. 1217–1227, Sep. 2001.

[10] J. Wedel-Heinen et al., 'Optimat report OB_TG6_R002 rev. 8', 2006.

[11] M. J. Owen and J. R. Griffiths, ‘Evaluation of biaxial stress failure surfaces for a glass fabric reinforced polyester resin under static and fatigue loading’, *J Mater Sci*, vol. 13, no. 7, pp. 1521–1537, Jul. 1978.
[12] T. P. Philippidis and A. P. Vassilopoulos, ‘Complex stress state effect on fatigue life of GRP laminates.: part I, experimental’, *International Journal of Fatigue*, vol. 24, no. 8, pp. 813–823, Aug. 2002.
[13] M. Quaresimin, L. Susmel, and R. Talreja, ‘Fatigue behaviour and life assessment of composite laminates under multiaxial loadings’, *International Journal of Fatigue*, vol. 32, no. 1, pp. 2–16, Jan. 2010.
[14] N. L. Post, J. Cain, K. J. McDonald, S. W. Case, and J. J. Lesko, ‘Residual strength prediction of composite materials: Random spectrum loading’, *Engineering Fracture Mechanics*, vol. 75, no. 9, pp. 2707–2724, Jun. 2008.
[15] Y. A. Dzenis, ‘Cycle-based analysis of damage and failure in advanced composites under fatigue: 1. Experimental observation of damage development within loading cycles’, *International Journal of Fatigue*, vol. 25, no. 6, pp. 499–510, Jun. 2003.
[16] A. Plumtree, M. Melo, and J. Dahl, ‘Damage evolution in a [±45]2S CFRP laminate under block loading conditions’, *International Journal of Fatigue*, vol. 32, no. 1, pp. 139–145, Jan. 2010.
[17] J. F. Mandell and U. Meier, ‘Effects of Stress Ratio Frequency and Loading Time on the Fatigue. Behaviour of Glass-Reinforced Epoxy’, in *Long-term behavior of composites: a symposium*, ASTM International, 1983.
[18] D. Hull and T. W. Clyne, *An Introduction to Composite Materials*, 2nd ed. Cambridge University Press, 1996.
[19] J. Tong, F. J. Guild, S. L. Ogin, and P. A. Smith, ‘On matrix crack growth in quasi-isotropic laminates--I. Experimental investigation’, *Composites Science and Technology*, vol. 57, no. 11, pp. 1527–1535, 1997.
[20] M. D. Gilchrist, ‘The fatigue performance of composite structural components’, in *Fatigue in composites: science and technology of the fatigue response of fibre-reinforced plastics*, Woodhead Publishing, 2003.
[21] H. Mao and S. Mahadevan, ‘Fatigue damage modelling of composite materials’, *Composite Structures*, vol. 58, no. 4, pp. 405–410, Dec. 2002.
[22] J. Tong, ‘Characteristics of fatigue crack growth in GFRP laminates’, *International Journal of Fatigue*, vol. 24, no. 2–4, pp. 291–297.
[23] R. Nijssen, ‘Fatigue and residual strength of rotor blade materials’, in *European wind energy conference proceedings EWEC 2006*, .
[24] C. Kassapoglou, ‘Fatigue of composite materials under spectrum loading’, *Composites Part A: Applied Science and Manufacturing*, vol. 41, no. 5, pp. 663–669, May 2010.
[25] M. J. Khan, G. Bhuyan, M. T. Iqbal, and J. E. Quaicoe, ‘Hydrokinetic energy conversion systems and assessment of horizontal and vertical axis turbines for river and tidal applications: A technology status review’, *Applied Energy*, vol. 86, no. 10, pp. 1823–1835, Oct. 2009.
[26] W. M. J. Batten, A. S. Bahaj, A. F. Molland, and J. R. Chaplin, ‘Experimentally validated numerical method for the hydrodynamic design of horizontal axis tidal turbines’, *Ocean Engineering*, vol. 34, no. 7, pp. 1013–1020, May 2007.
[27] A. S. Bahaj, A. F. Molland, J. R. Chaplin, and W. M. J. Batten, ‘Power and thrust measurements of marine current turbines under various hydrodynamic flow conditions in a cavitation tunnel and a towing tank’, *Renewable Energy*, vol. 32, no. 3, pp. 407–426, Mar. 2007.

[28] R. E. Wilson, 'Aerodynamic Behavior of Wind Turbines', in *Wind Turbine Technology: Fundamental Concepts of Wind Turbine Engineering*, American Society of Mechanical Engineers, 1994.
[29] J. Van Briel and J. Van Leuven, 'A 2-D flow model for the horizontal axis wind turbine', in *Wind Energy Conversion 1984: Proceedings of the Sixth BWEA Wind Energy Conference University of Reading, 28-30 March 1984*, Cambridge University Press, 1985.
[30] P. P. Friedmann, 'Aeroelastic stability and response analysis of large horizontal-axis wind turbines', *Journal of Wind Engineering and Industrial Aerodynamics*, vol. 5, no. 3–4, pp. 373–401, May 1980.
[31] R. Carr, Personal Communication, 'Tide Height Data'. The Marine Institute, Galway, Ireland, Jul-2010.
[32] A. G. Bryans, B. Fox, P. A. Crossley, and M. O'Malley, 'Impact of tidal generation on power system operation in Ireland', *Power Systems, IEEE Transactions on*, vol. 20, no. 4, pp. 2034–2040, 2005.
[33] D. T. Pugh, *Tides, Surges, and Mean Sea-Level/a Handbook for Engineers and Scientists*. John Wiley & Sons Inc, 1988.
[34] W. M. J. Batten, A. S. Bahaj, A. F. Molland, and J. R. Chaplin, 'Hydrodynamics of marine current turbines', *Renewable Energy*, vol. 31, no. 2, pp. 249–256, Feb. 2006.
[35] F. Bertagnolio, N. S_rensen, J. Johansen, and P. Fuglsang, 'Wind Turbine Airfoil Catalogue', Riso_ National Laboratory, Roskilde, Denmark, Ris_o-R-1280(EN), Aug. 2001.
[36] C. W. Kensche, 'Fatigue of composites for wind turbines', *International Journal of Fatigue*, vol. 28, no. 10, pp. 1363–1374, Oct. 2006.
[37] R. J. Crawford, *Plastics Engineering*. Butterworth-Heinemann, 1998.
[38] B. D. Agarwal and L. J. Broutman, *Analysis and Performance of Fiber Composites, 2nd Edition*, 2nd ed. Wiley-Interscience, 1990.
[39] R. W. Thresher, L. P. Mirandy, T. C. Carne, and D. W. Lobitz, 'Structural dynamic behaviour of wind turbines', in *Wind Turbine Technology: Fundamental Concepts of Wind Turbine Engineering*, American Society of Mechanical Engineers, 1994.
[40] N. Barltrop, K. S. Varyani, A. Grant, D. Clelland, and X. Pham, 'Wave-current interactions in marine current turbines', *Proceedings of the Institution of Mechanical Engineers, Part M: Journal of Engineering for the Maritime Environment*, vol. 220, no. 4, pp. 195 –203, Dec. 2006.
[41] Det Norske Veritas., 'DNV-OS-J102, Design and Manufacture of Wind Turbine Blades'. Oct-2006.
[42] N. L. Post, S. W. Case, and J. J. Lesko, 'Modeling the variable amplitude fatigue of composite materials: A review and evaluation of the state of the art for spectrum loading', *International Journal of Fatigue*, vol. 30, no. 12, pp. 2064–2086, Dec. 2008.
[43] D. A. Spera, *Wind Turbine Technology: Fundamental Concepts of Wind Turbine Engineering*. American Society of Mechanical Engineers, 1994.

Table 1 (a) Epoxy / E-glass material properties

Inputs		**Single unidirectional ply properties**		**Quasi-isotropic laminate** $[(45\backslash135\backslash90\backslash0)_2]_s$	
V_f	50%	E_1	38 GPa	E_x, E_y	19.3 GPa
E_f	72.4 GPa	E_2	11.5 GPa	G_{xy}	7.2 GPa
v_f	0.22	G_{12}	3.5 GPa	v_{xy}	0.330
E_m	3.5 GPa	v_{12}	0.285		
v_m	0.35				

Table 1 (b) Vinyl ester / E-glass material properties

Inputs		**Single unidirectional ply properties**		**Quasi-isotropic laminate** $[(45\backslash135\backslash90\backslash0)_2]_s$	
V_f	50%	E_1	37.9 GPa	E_x, E_y	19.1 GPa
E_f	72.4 GPa	E_2	11.3 GPa	G_{xy}	7.2 GPa
v_f	0.22	G_{12}	3.4 GPa	v_{xy}	0.330
E_m	3.4 GPa	v_{12}	0.285		
v_m	0.35				

Table 2 Constants for power law fit to fatigue data

Material	**Coefficient (*A*)**	**Exponent (*B*)**
Epoxy / E-glass R = 0.1	0.02830	0.0863
Epoxy / E-glass R = 0.5	0.03507	0.0863
Vinyl ester / E-glass R = 0.1	0.02908	0.1063
Vinyl ester / E-glass R = 0.5	0.03704	0.1063

Table 3 Parameters for base case hydrodynamic model

Parameter	**Value**
Water velocity	2.6 m/s
Number of blades	3
R_{outer}	5 m
RPM	16
C_L	1.0
L/D	70
Angle of attack	7°
ζ	0.333
Water density	1025 kg/m^3
Water viscosity	0.0013155 Pa.s
R_{inner}	1.5 m

Table 4 Parameters for fatigue reference case

Parameter	**Value**
Maximum water velocity	4.0 m/s
Neap max. velocity / Spring max. velocity	60%
Factor of safety applied to loads	2
Tower shadow	50%
Control system	PR
Material	Epoxy / E-glass
Main spar top cap thickness range	35 mm – 6 mm
Shear web and fairing thickness range	12 mm – 4 mm

FIGURES

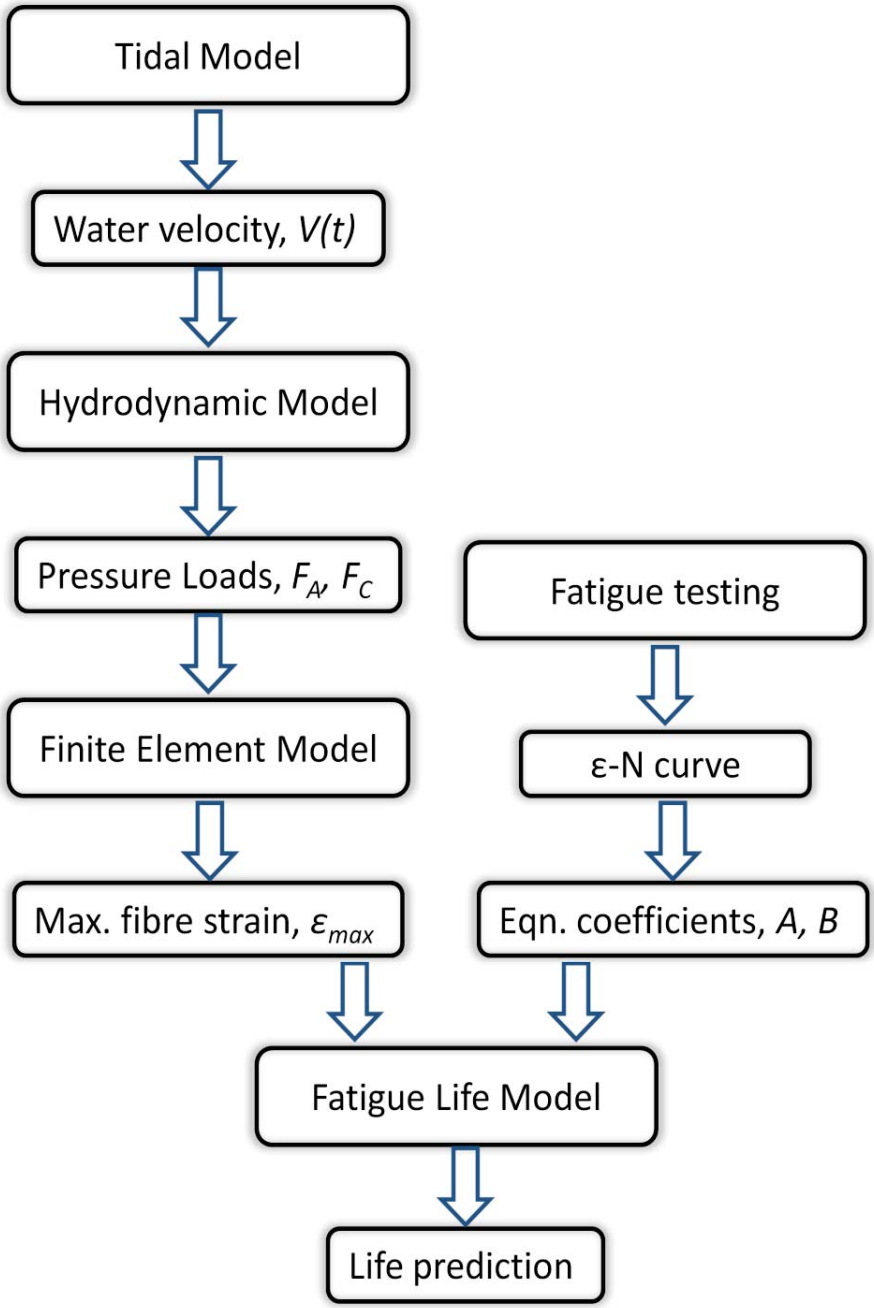

Figure 1 Flowchart of fatigue life calculation methodology

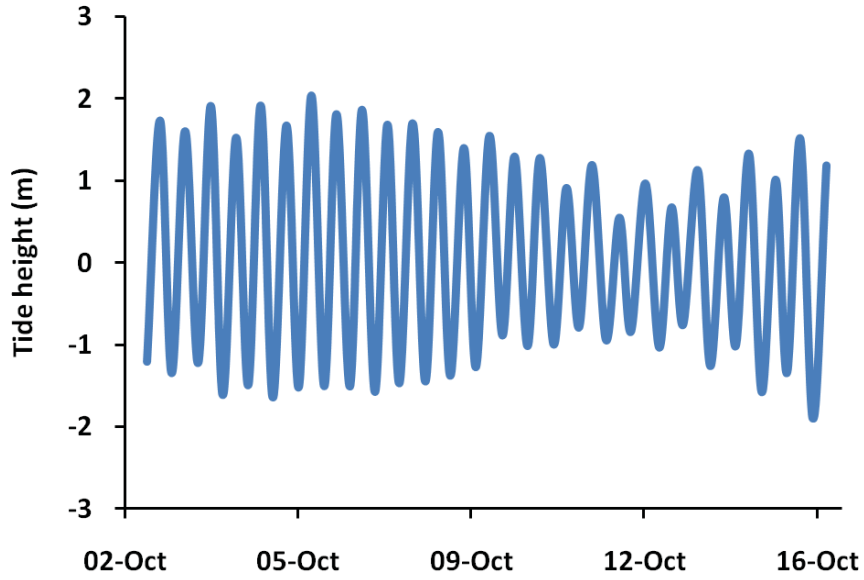

(a) tide height data

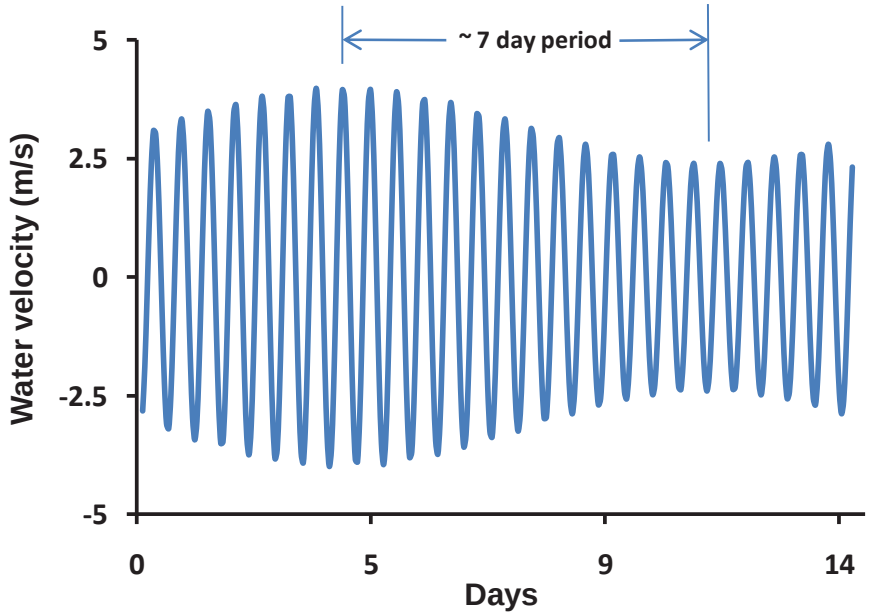

(b) sinusoidal model output

Figure 2 (a) Typical tidal pattern around Ireland [31], and (b) sinusoidal model for water velocity

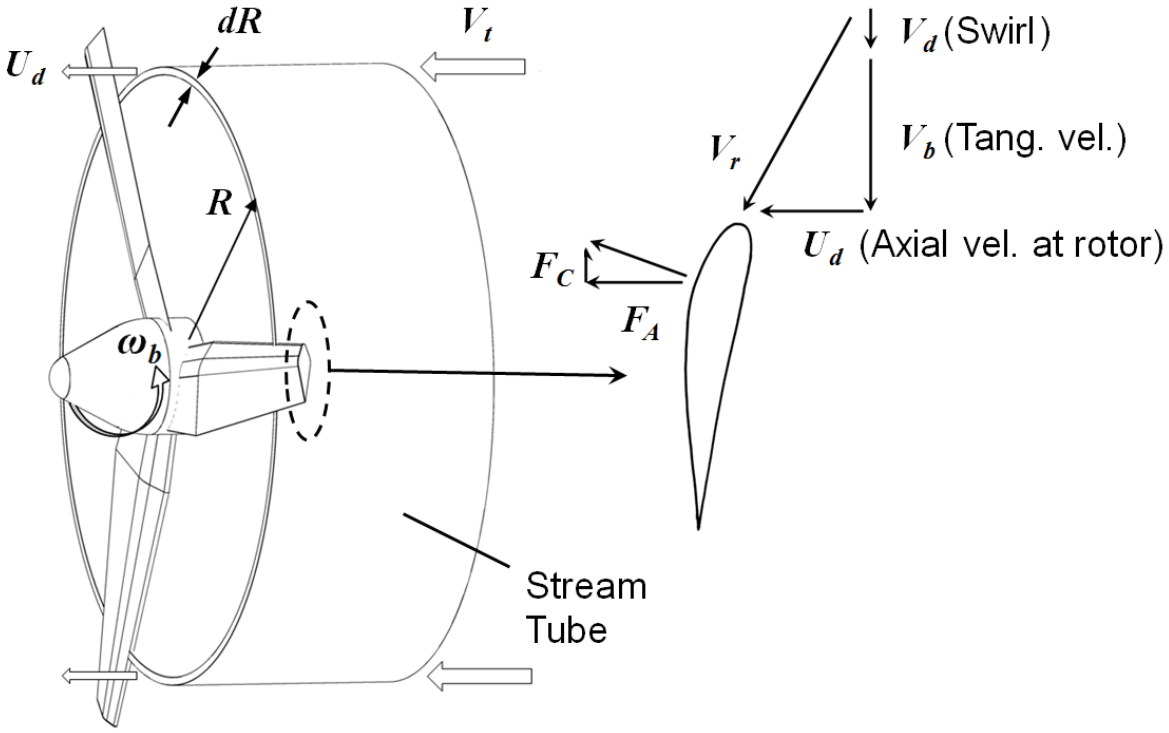

Figure 3 Schematic of stream tube concept

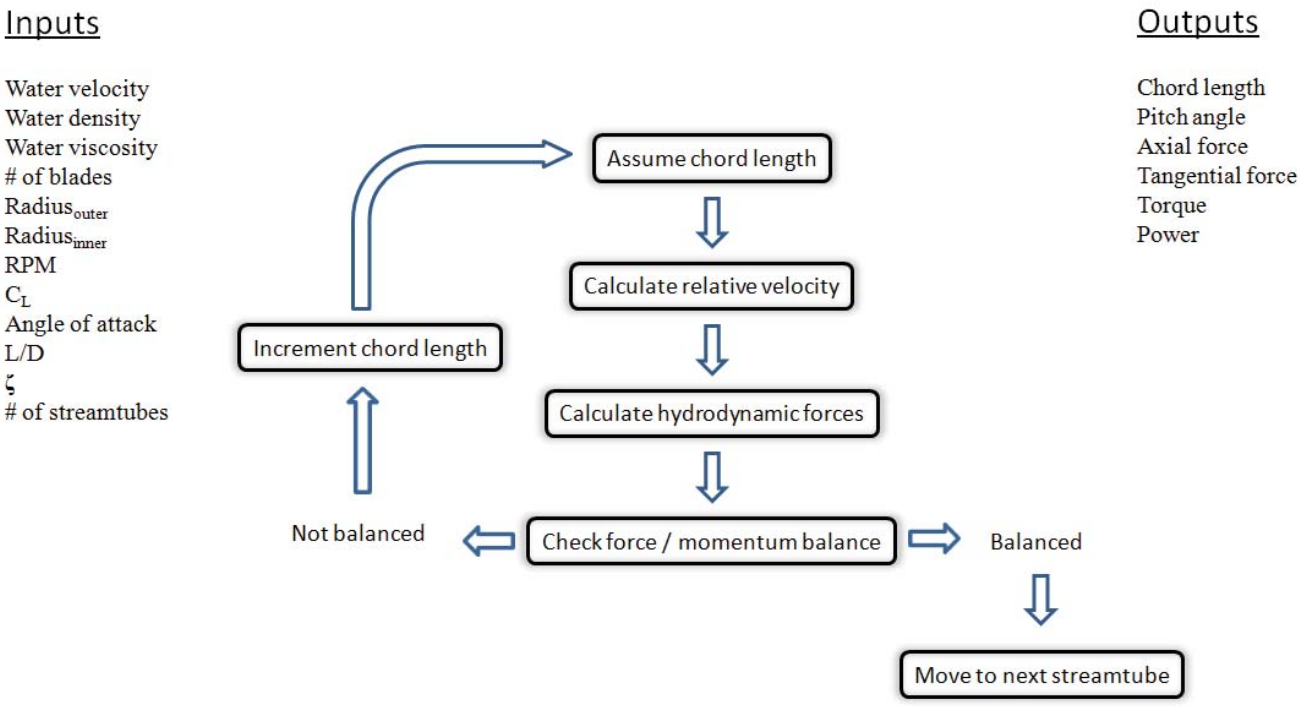

Figure 4 Summary of hydrodynamic model

Figure 5 Cross section view of RISO-A1-24 airfoil

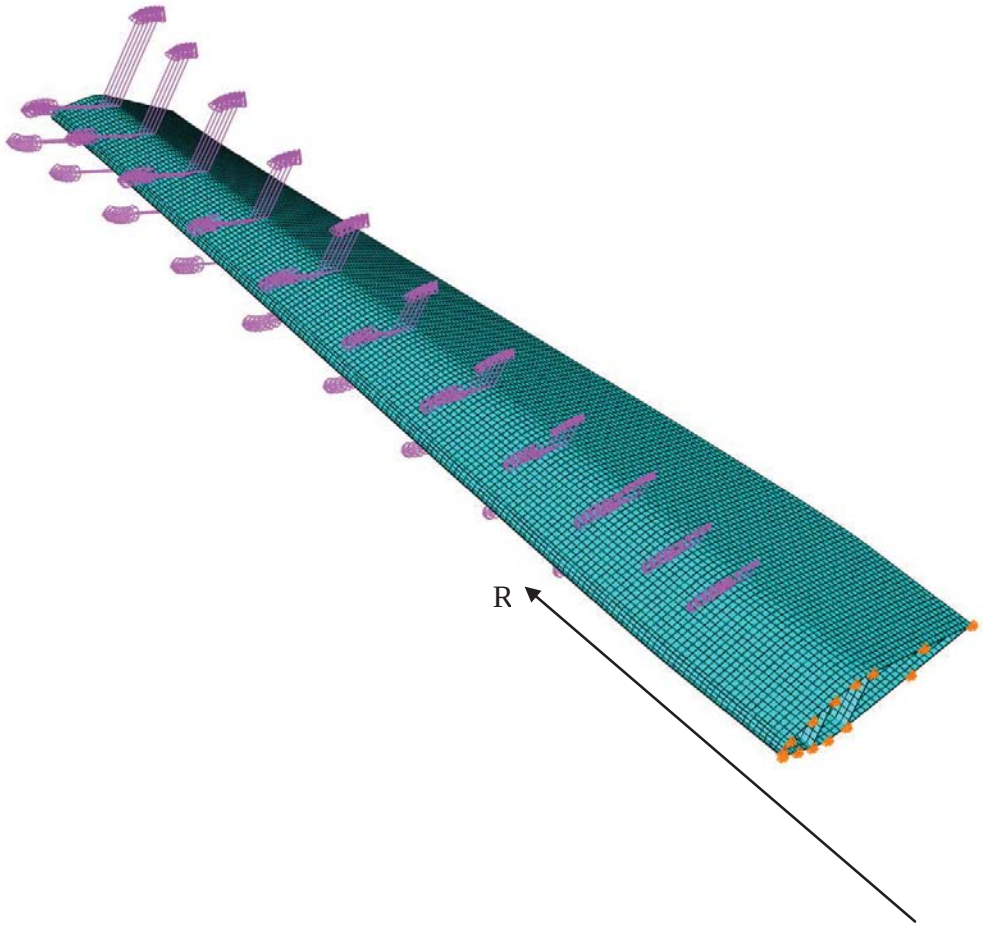

Figure 6 Finite element model of 5m tidal turbine blade for a 3-bladed, 330kW at 2.6m/s current velocity

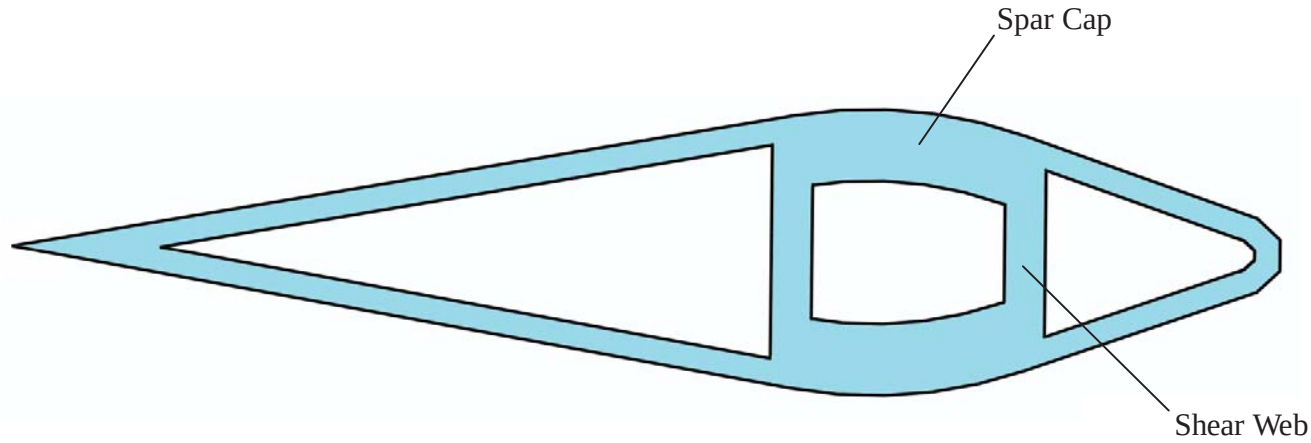

Figure 7 Simplified aerofoil shape used for finite element analysis of blade

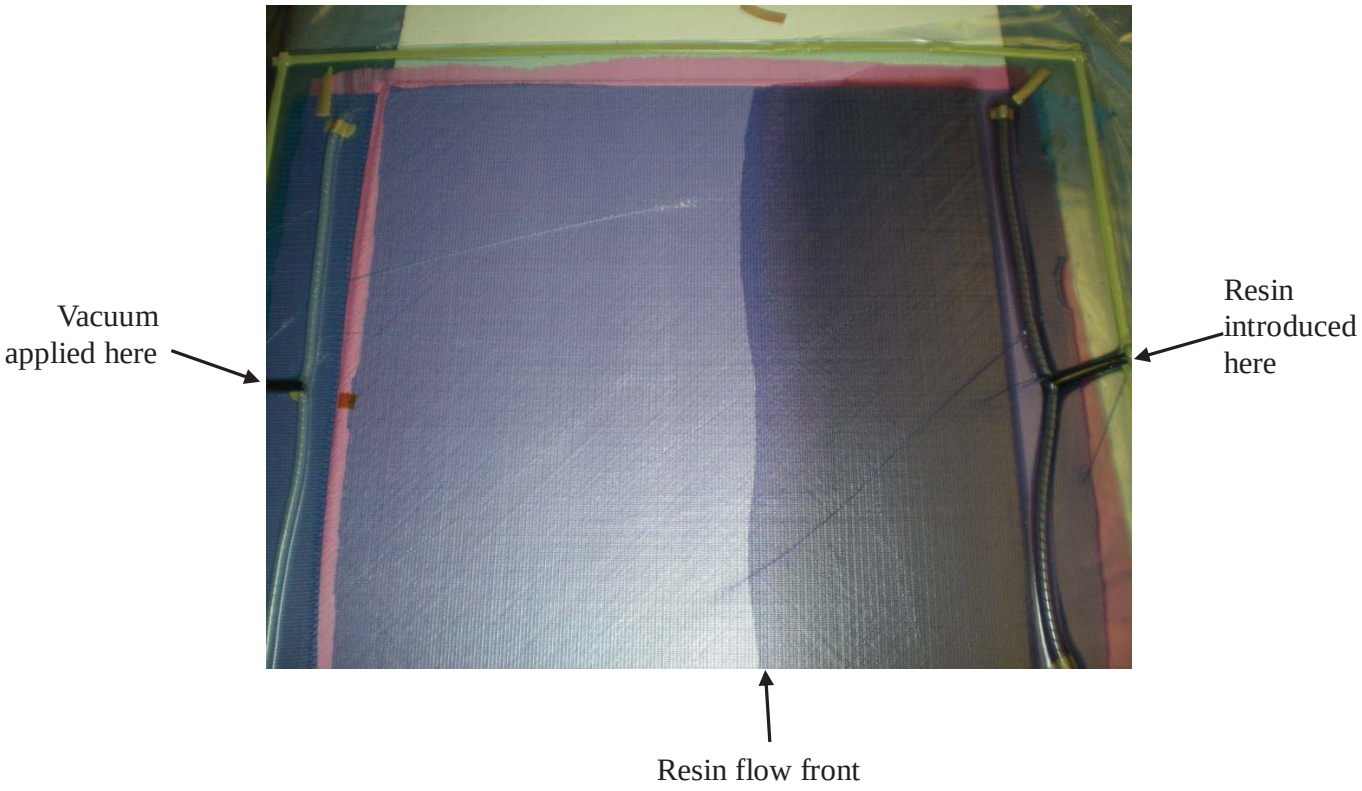

Figure 8 Laminates being manufactured by vacuum assisted resin transfer moulding (VARTM) process

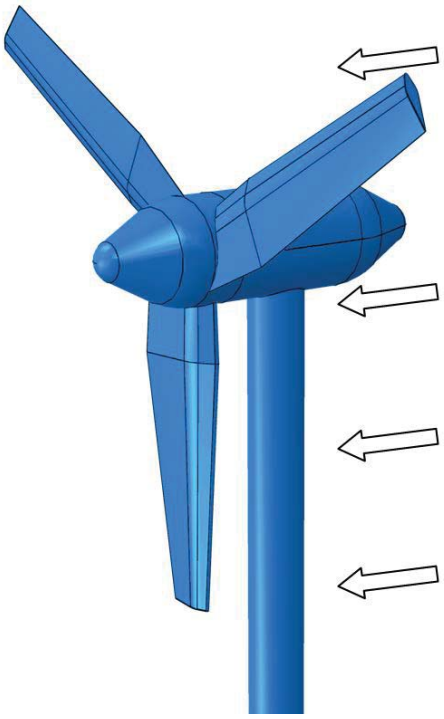

Figure 9 Tower shadow effect on downstream 3 bladed tidal turbine

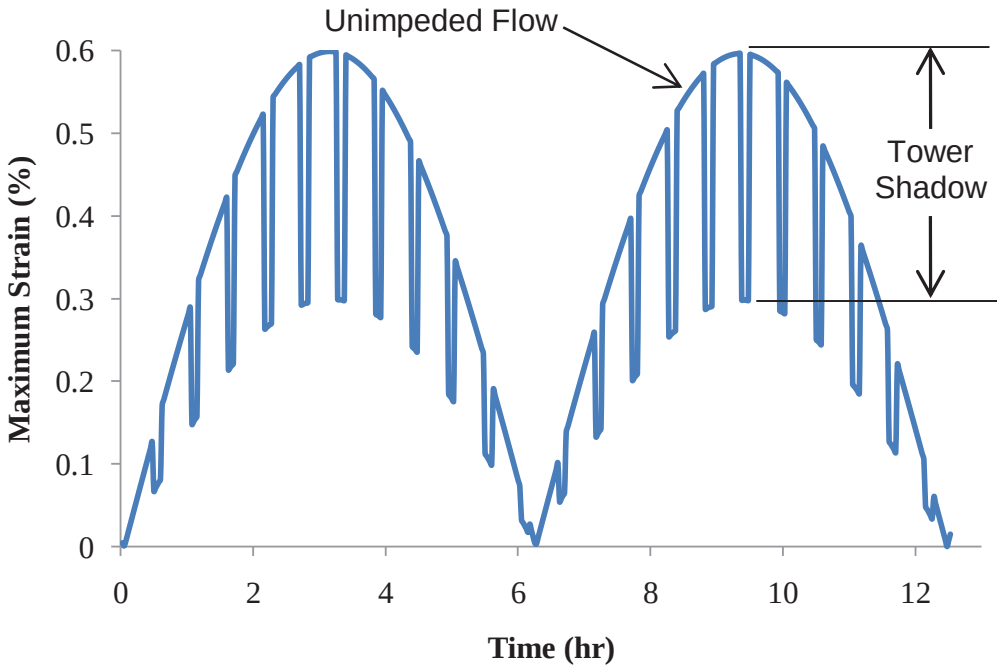

Figure 10 Schematic of effect of tower shadow effect (50%) on maximum strain in the turbine blade

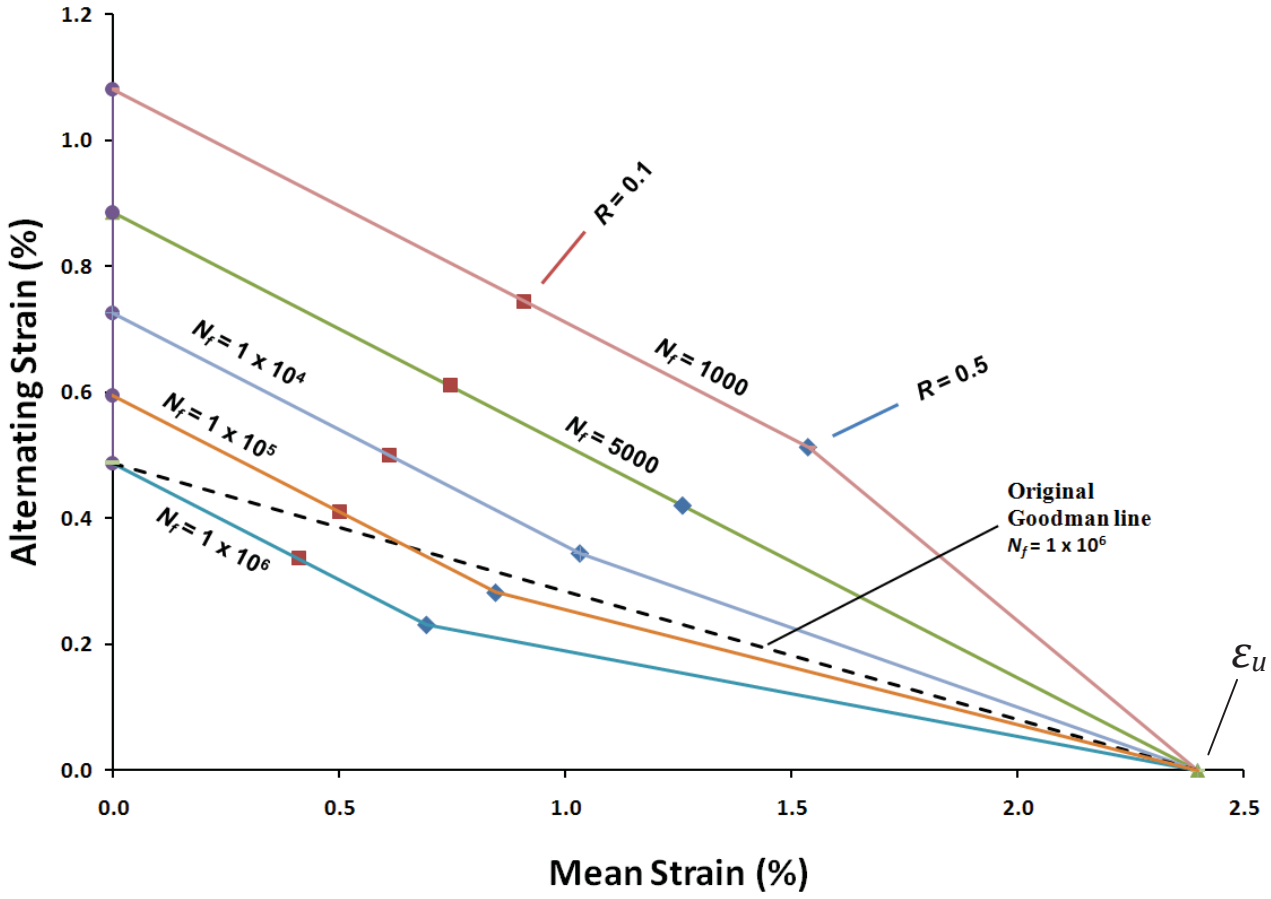

Figure 11 Schematic for constant life extrapolation from R = 0.1 test data to equivalent R = 0.5 data.

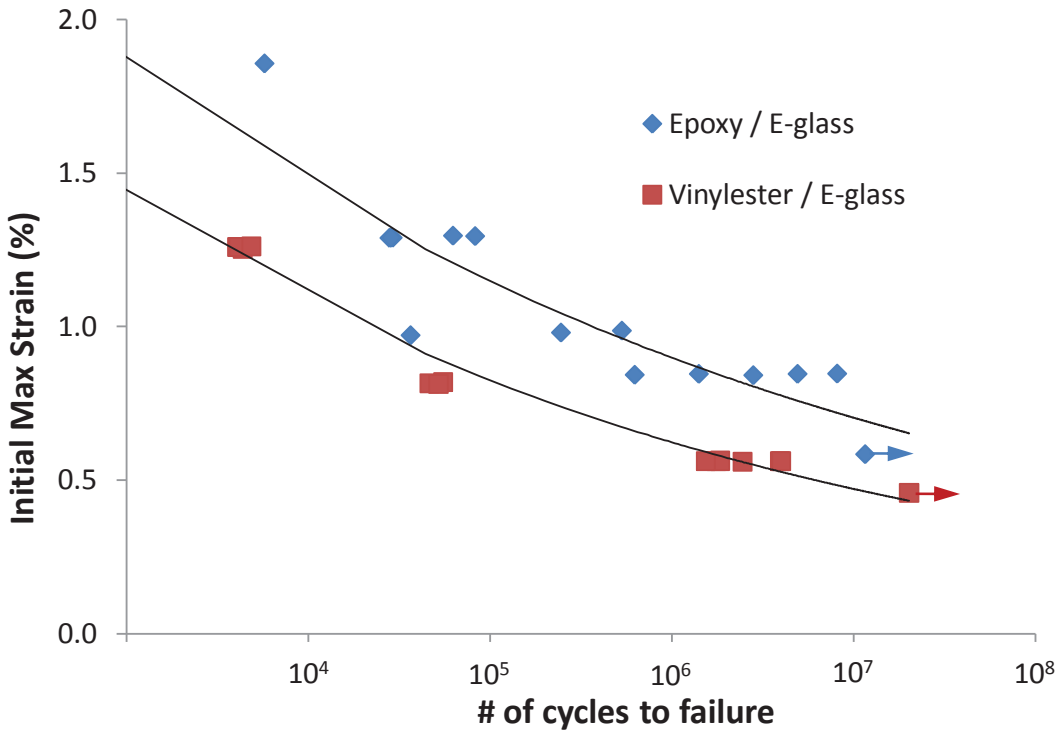

Figure 12 Test results for QI laminates (R = 0.1)

0.81% Initial strain, R = 0.1
# of cycles to failure 52,041
(a)

0.85% Initial strain, R = 0.1
# of cycles to failure 8,130,871
(b)

Figure 13 Post fatigue-test specimens of Vinyl ester (a) and Epoxy (b)

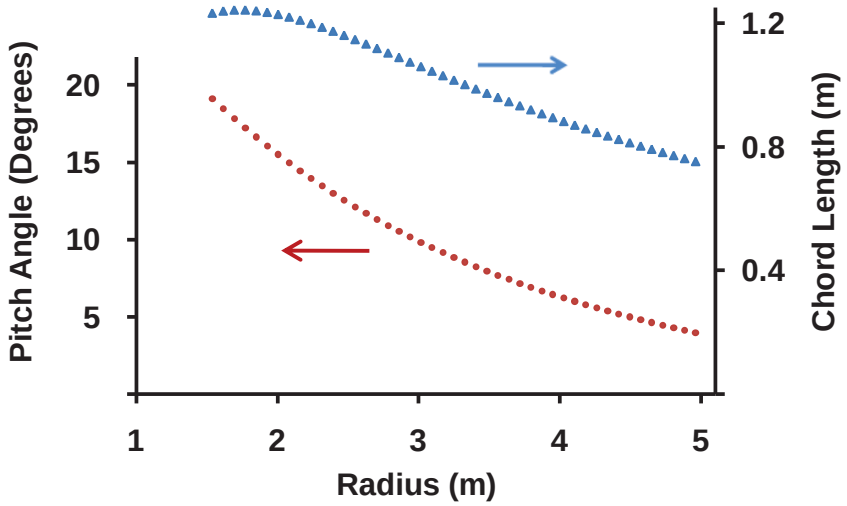

Figure 14 Radial distributions of blade pitch angle and chord length calculated using hydrodynamic model for 2.6 m/s water velocity

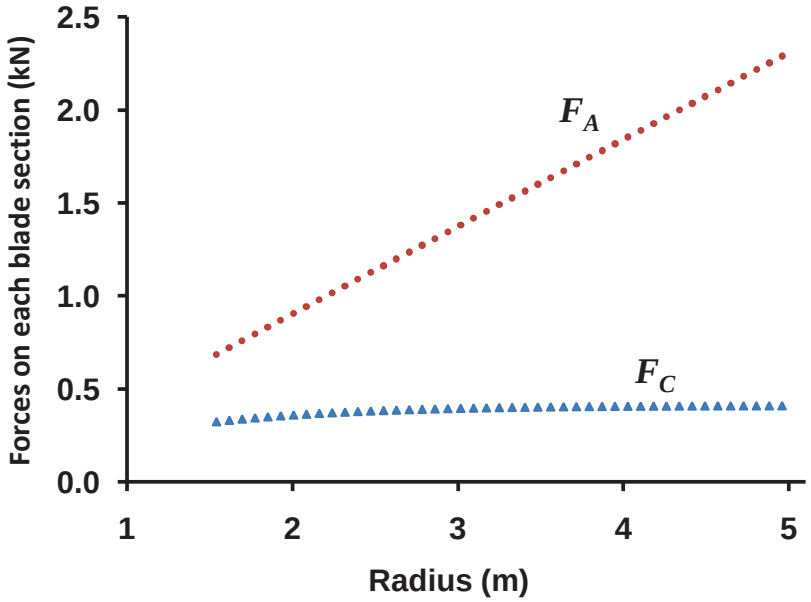

Figure 15 Radial distributions of axial (F_A) and tangential (F_C) forces from hydrodynamic model at 2.6 m/s water velocity

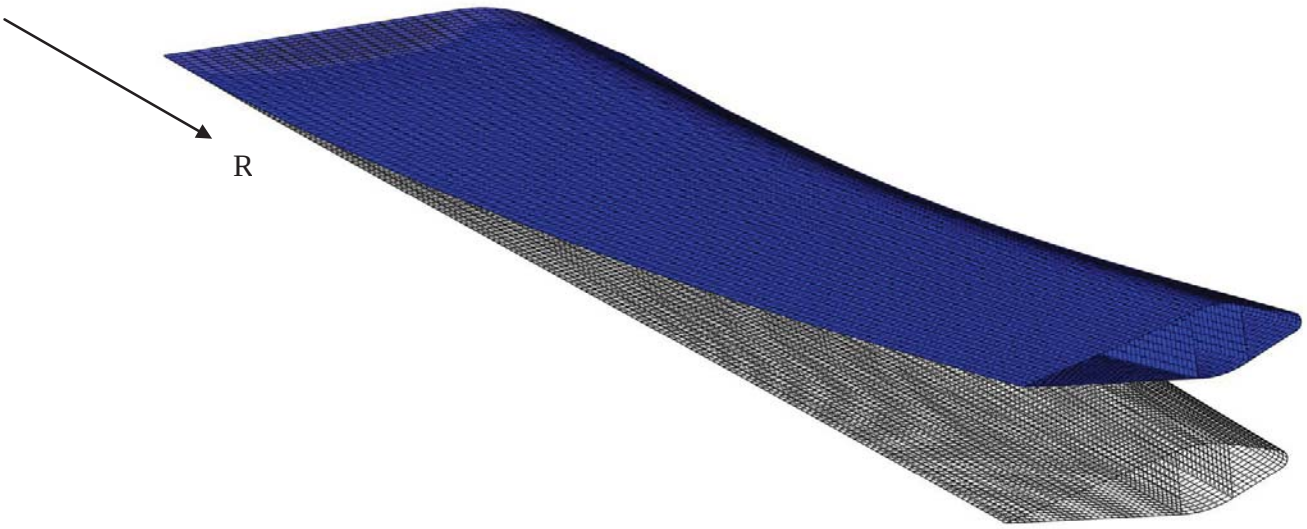

Figure 16 Undeformed and deformed shape of blade at 2.6 m/s water velocity, with a factor of safety of 2.0 applied.

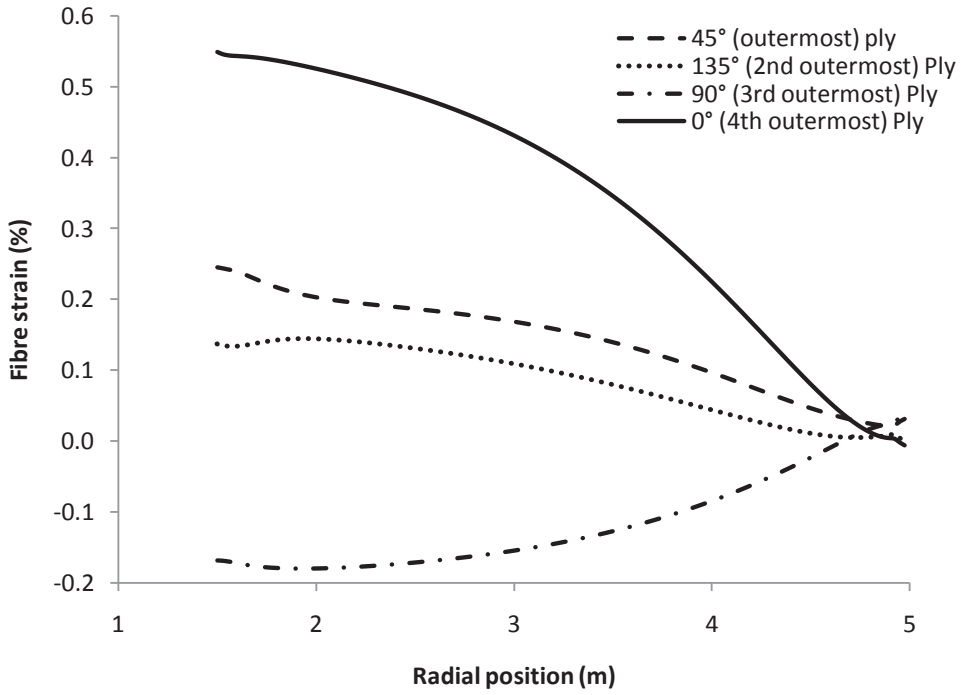

Figure 17 Fibre strains in the four outermost plies at maximum strain locations along blade operating in 2.6 m/s water velocity

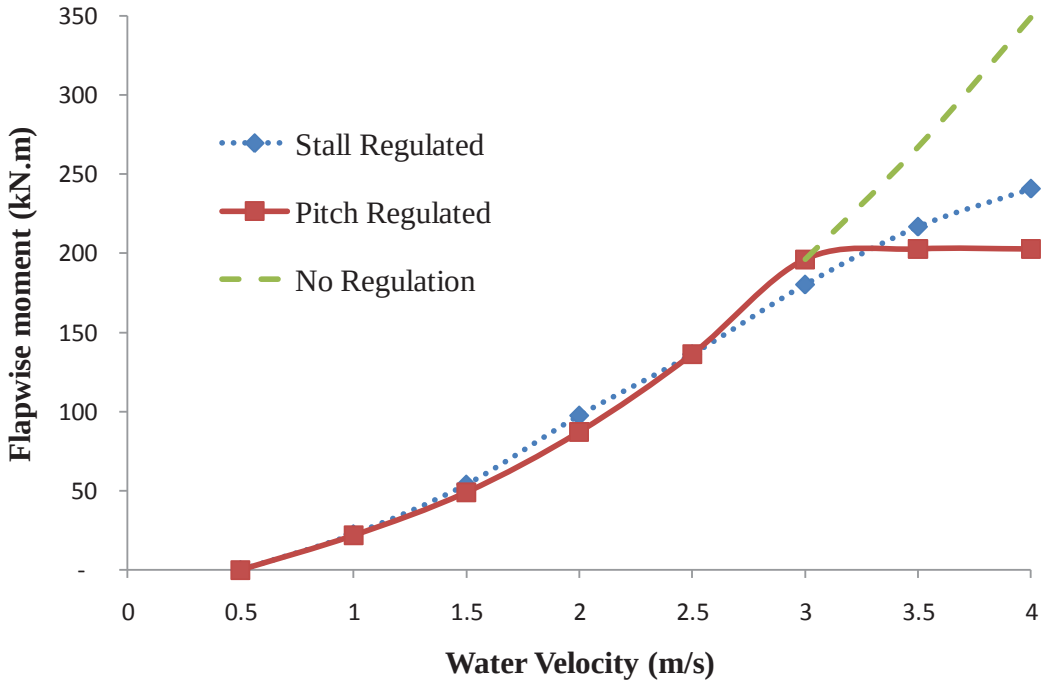

Figure 18 Predicted effect of water velocity on blade bending moment (at R = 1.5 m) for various control strategies, as calculated using hydrodynamic model

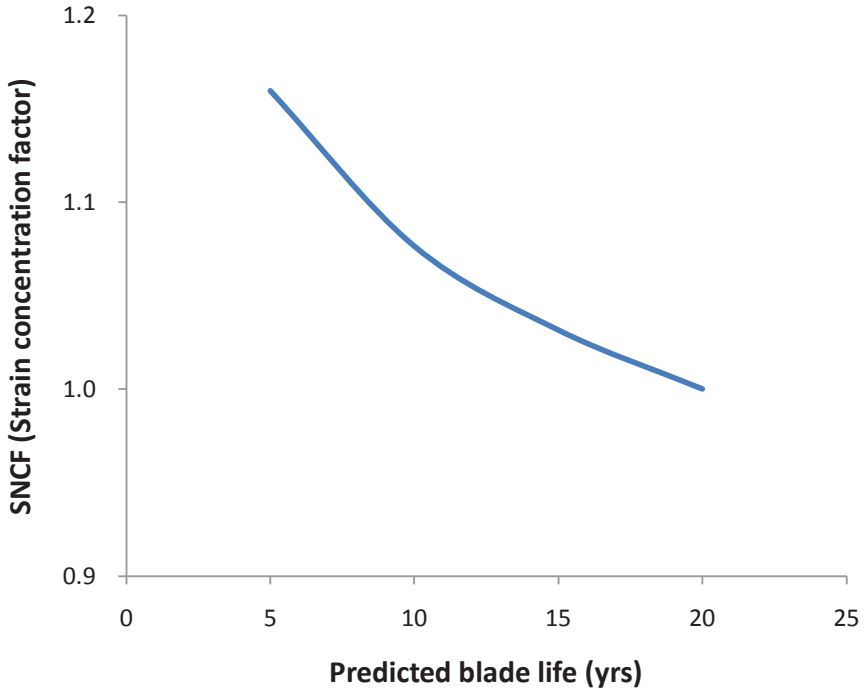

Figure 19 Predicted effect of stress concentrations on blade life for pitch regulated turbine in a tidal zone with 4.0 m/s maximum velocity and 60% neap/spring variation

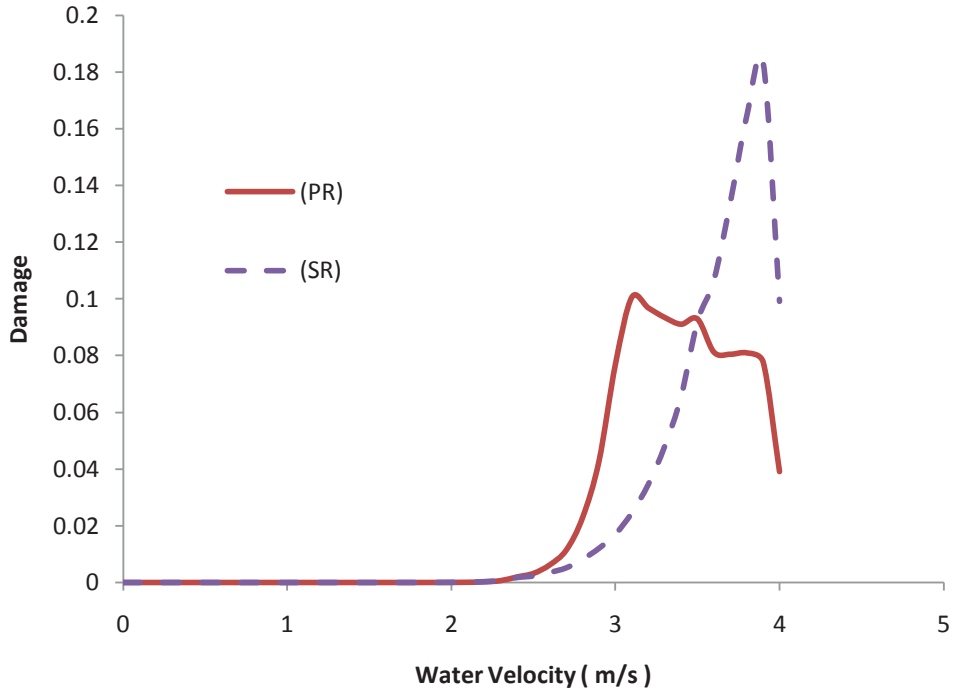

Figure 20. Damage accumulation pattern for pitch regulated (PR) and stall regulated (SR) epoxy/E-glass turbine blades running in a tidal zone with 4.0 m/s maximum velocity and 60% neap/spring variation.

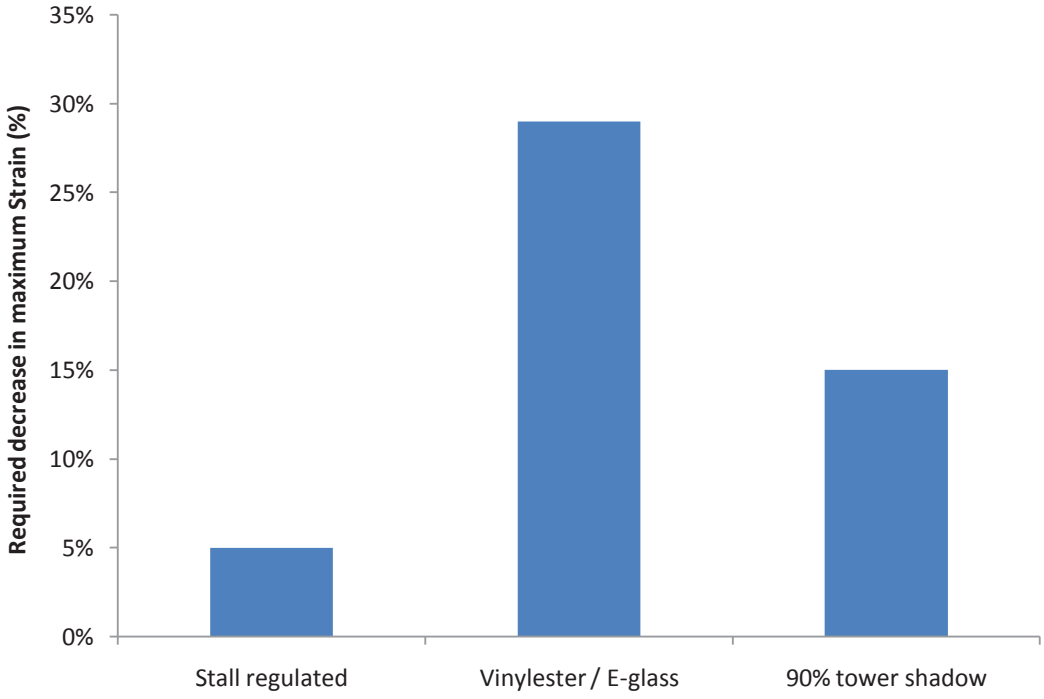

Figure 21. Comparison of required reductions in maximum strain due to various design changes, for a fatigue life equal to that of the reference case of Table 4.

Figure
Click here to download high resolution image

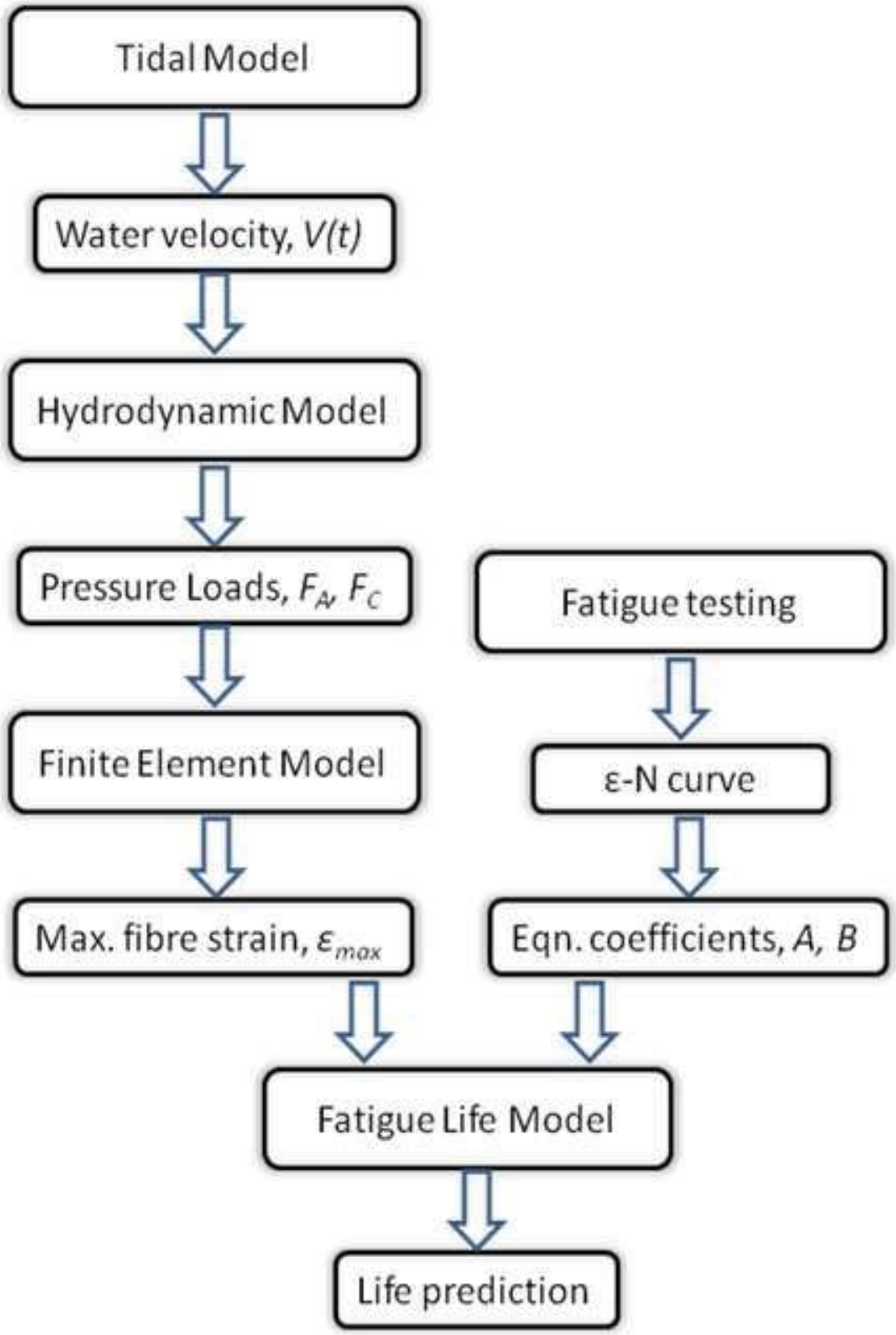

Figure 1 Flowchart of fatigue life calculation methodology

Figure
Click here to download high resolution image

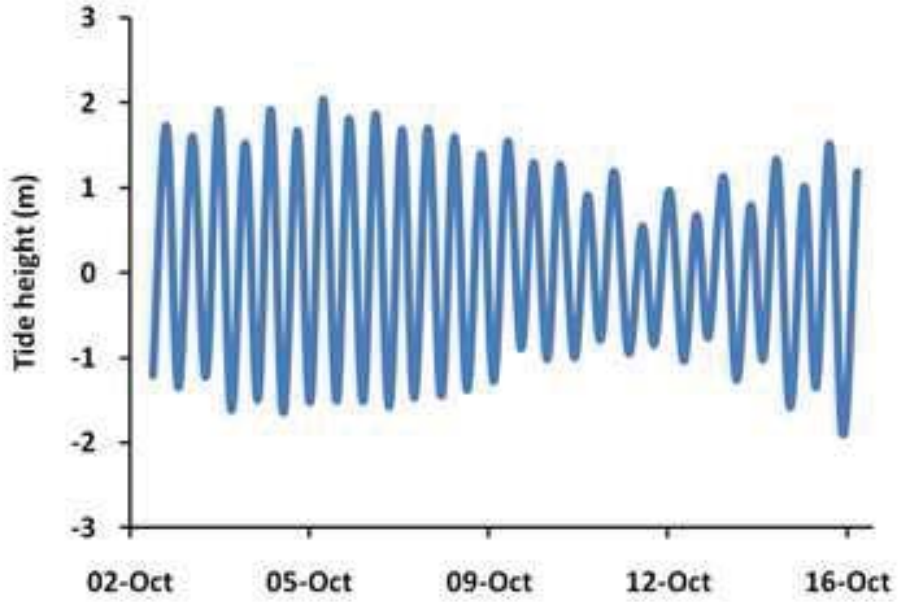

(a) tide height data

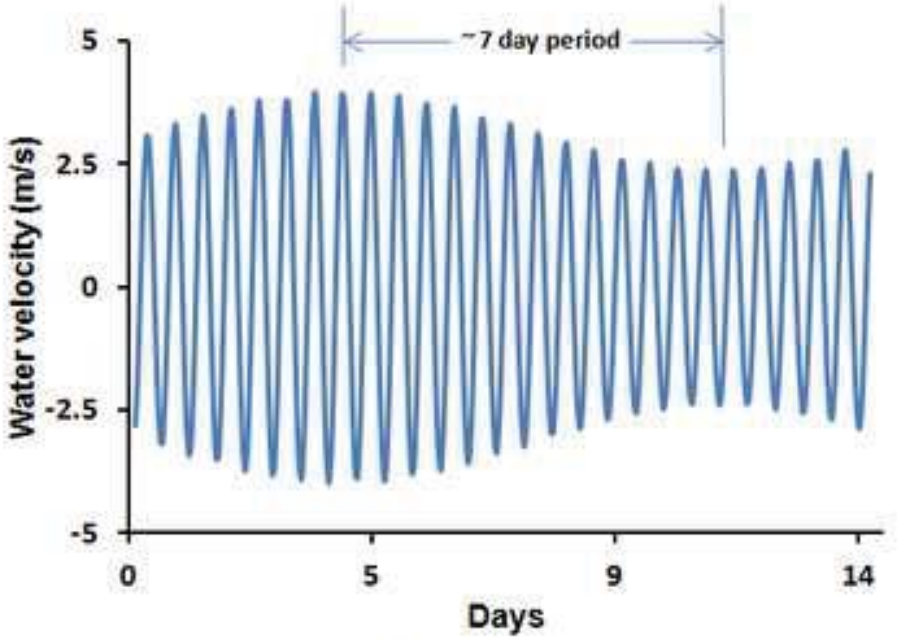

(b) sinusoidal model output

Figure 2 (a) Typical tidal pattern around Ireland [31], and (b) sinusoidal model for water velocity

Figure
Click here to download high resolution image

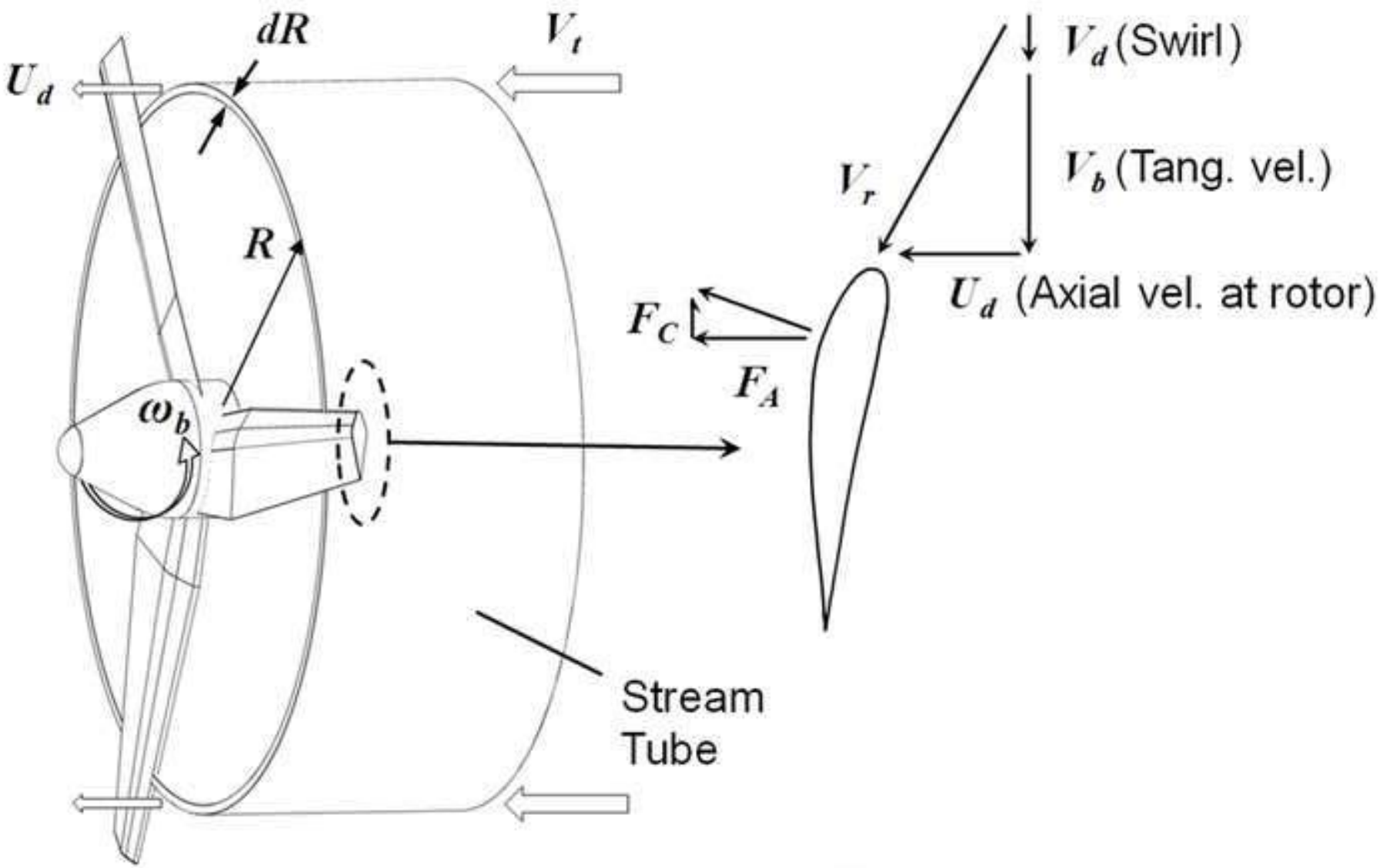

Figure 3 Schematic of stream tube concept

Figure
Click here to download high resolution image

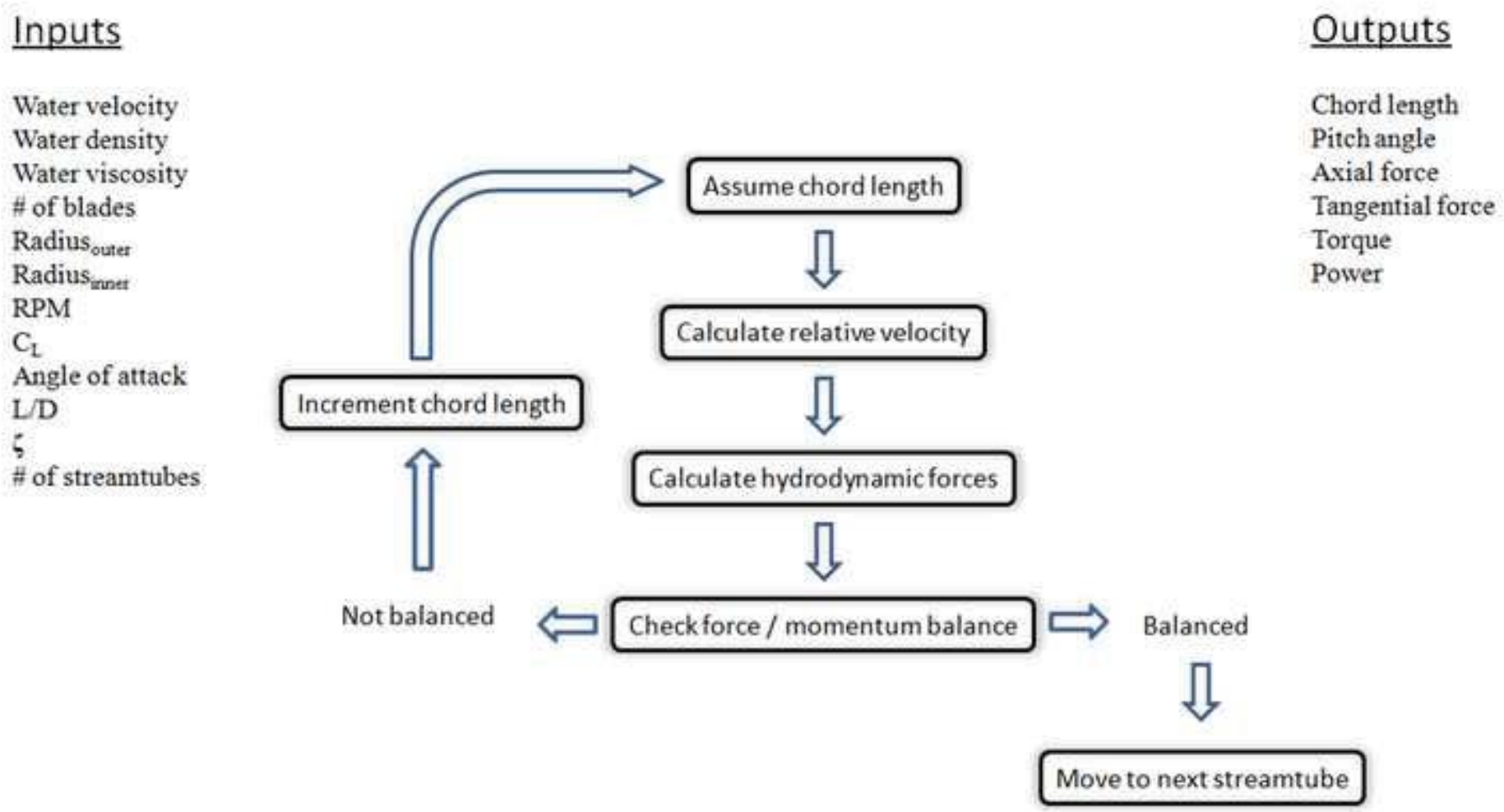

Figure 4 Summary of hydrodynamic model

Figure
Click here to download high resolution image

Figure 5 Cross section view of RISO-A1-24 airfoil

Figure
Click here to download high resolution image

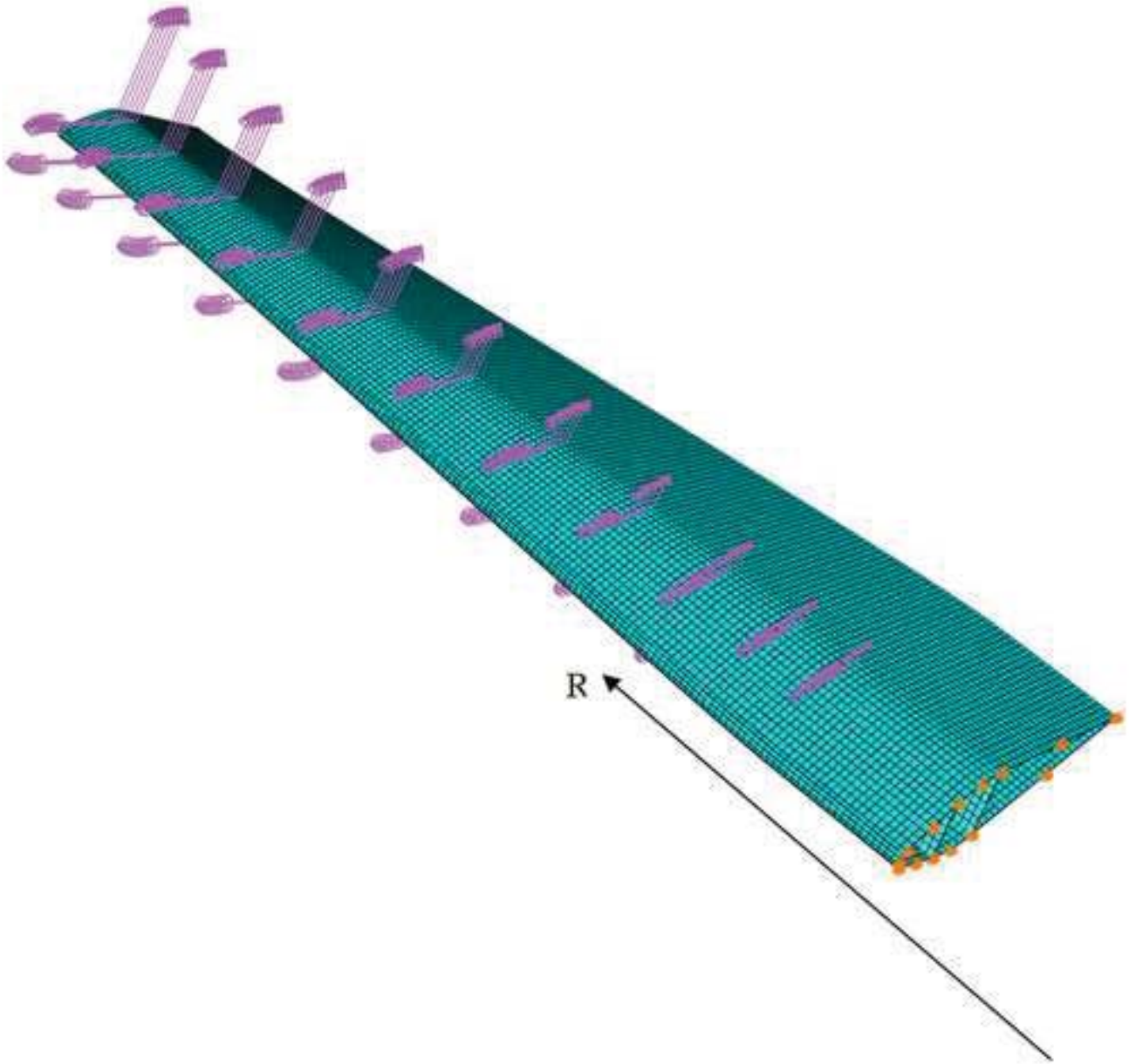

Figure 6 Finite element model of 5m tidal turbine blade for a 3-bladed, 330kW at 2.6m/s current velocity

Figure
Click here to download high resolution image

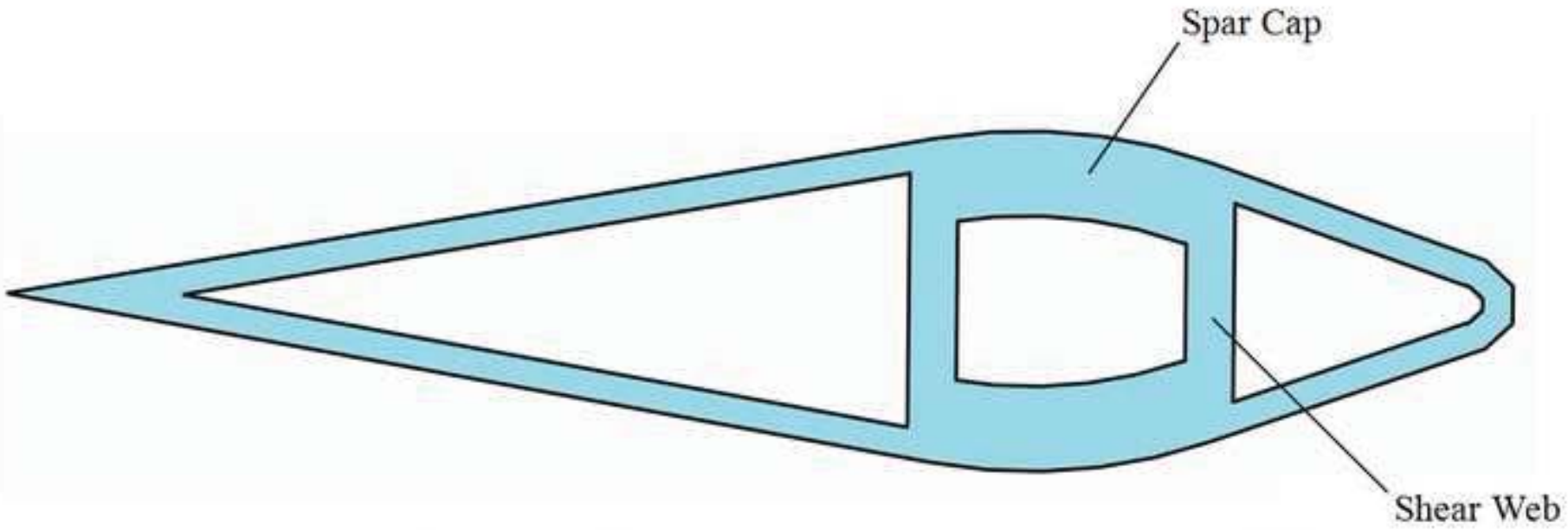

Figure 7 Simplified aerofoil shape used for finite element analysis of blade

Figure
Click here to download high resolution image

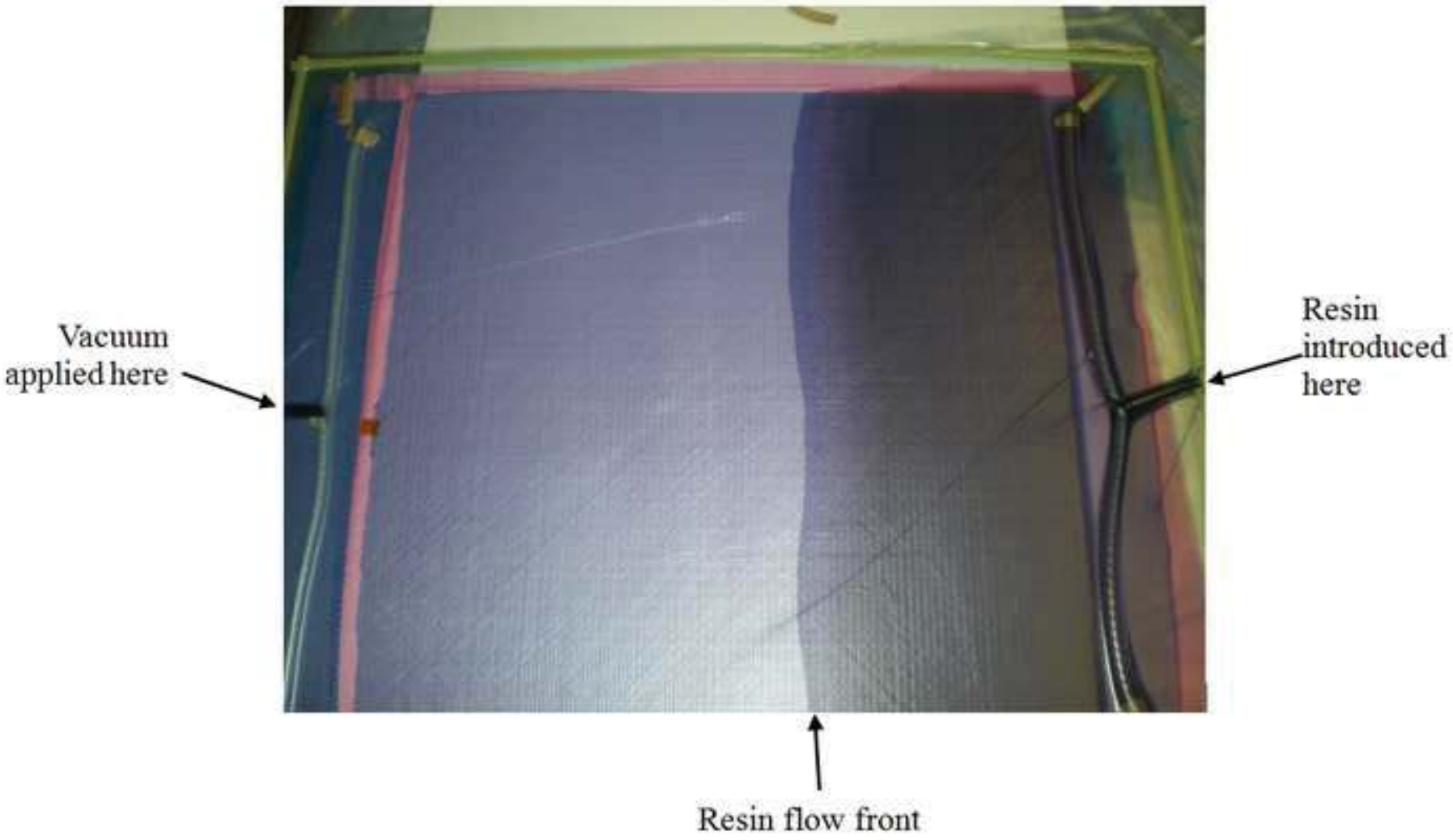

Figure 8 Laminates being manufactured by vacuum assisted resin transfer moulding (VARTM) process

Figure
Click here to download high resolution image

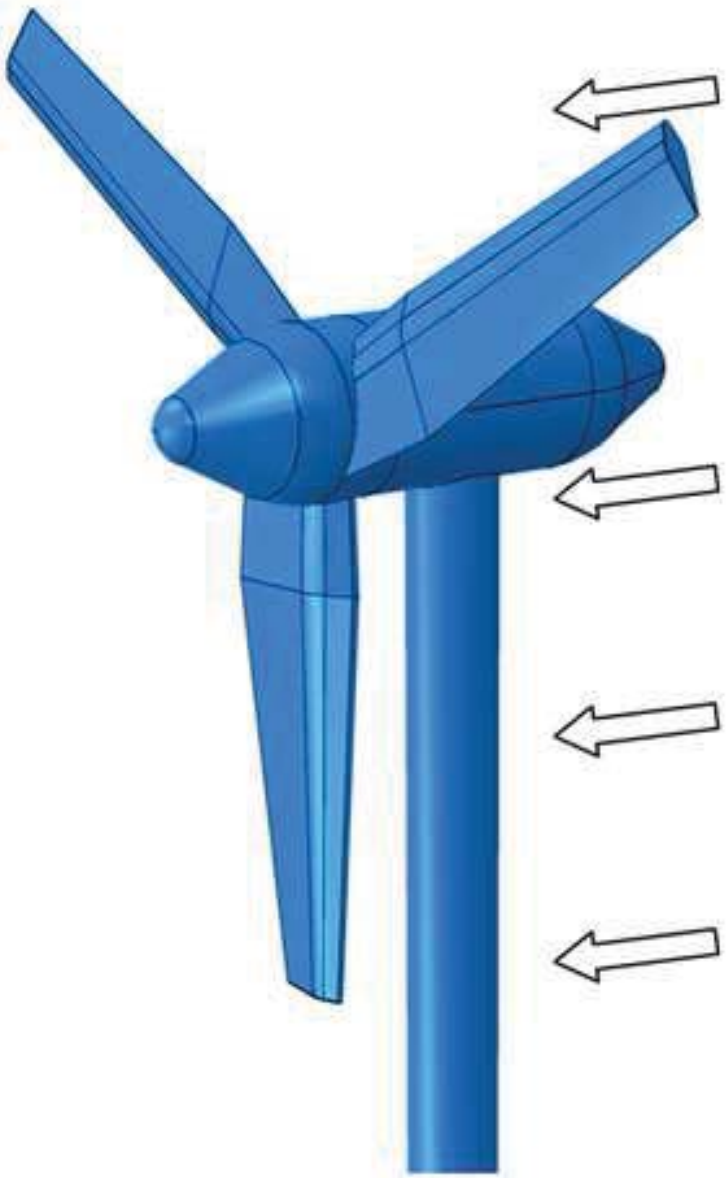

Figure 9 Tower shadow effect on downstream 3 bladed tidal turbine

Figure
Click here to download high resolution image

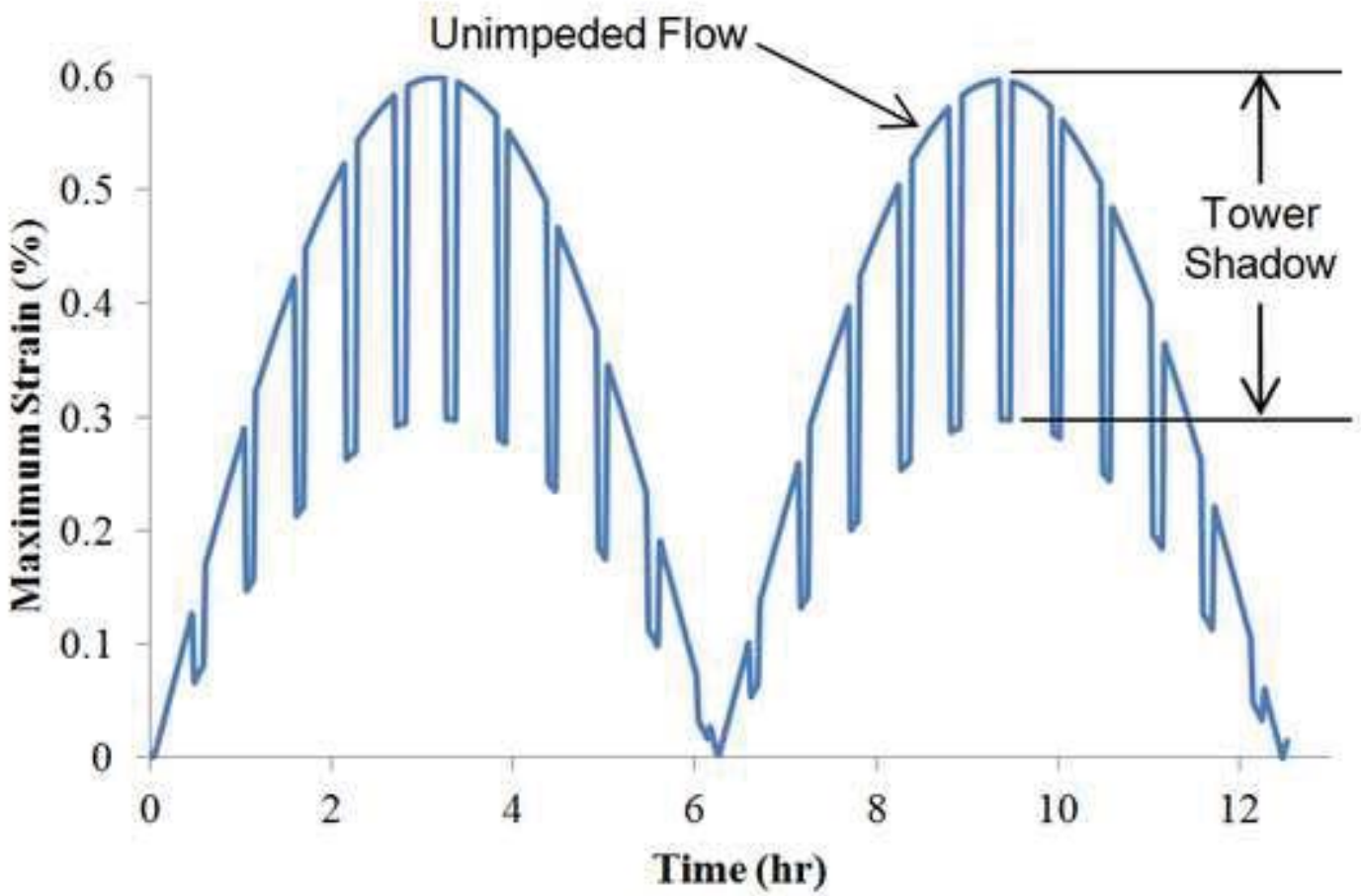

Figure 10 Schematic of effect of tower shadow effect (50%) on maximum strain in the turbine blade

Figure
Click here to download high resolution image

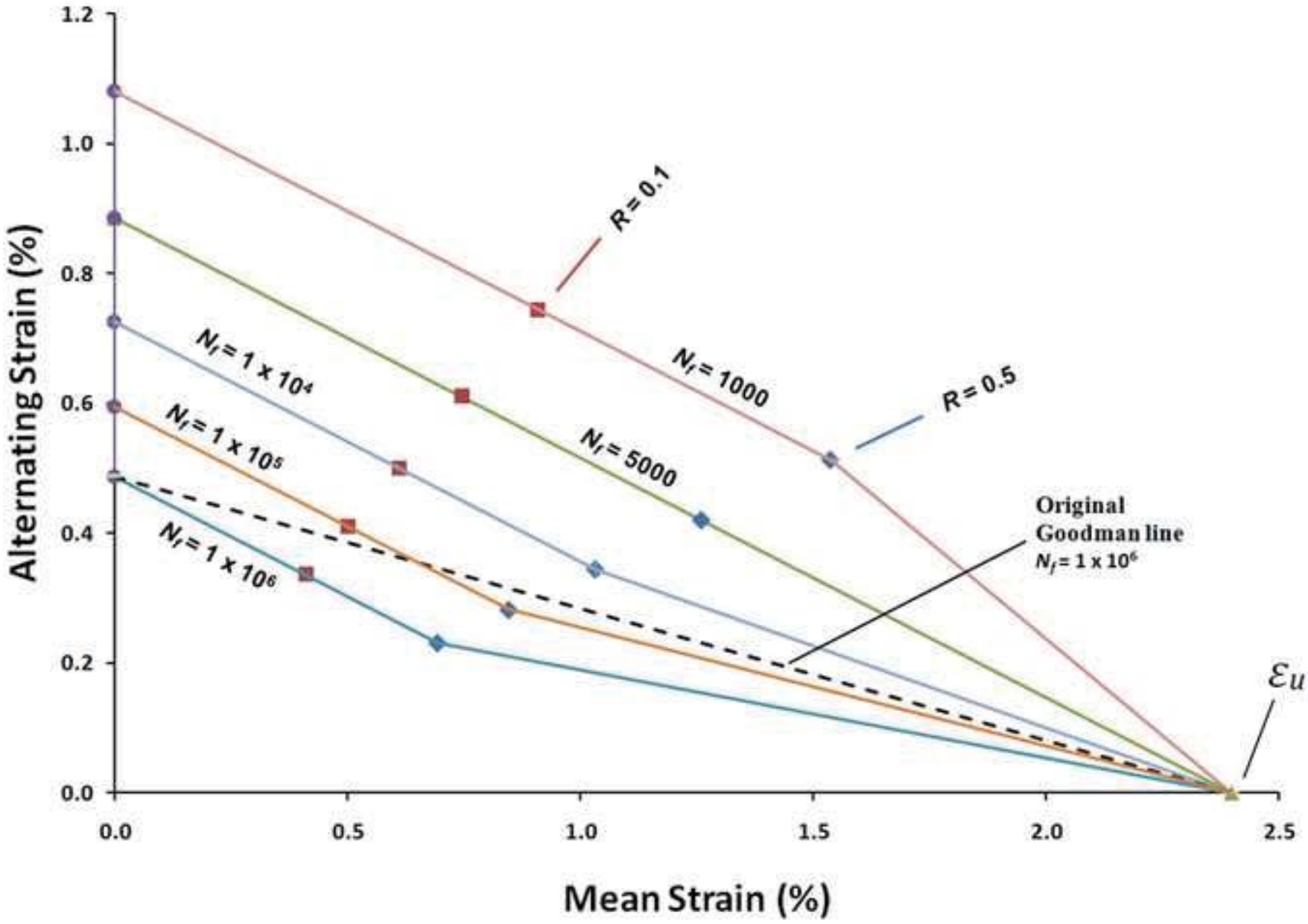

Figure 11 Schematic for constant life extrapolation from $R = 0.1$ test data to equivalent $R = 0.5$ data.

Figure
Click here to download high resolution image

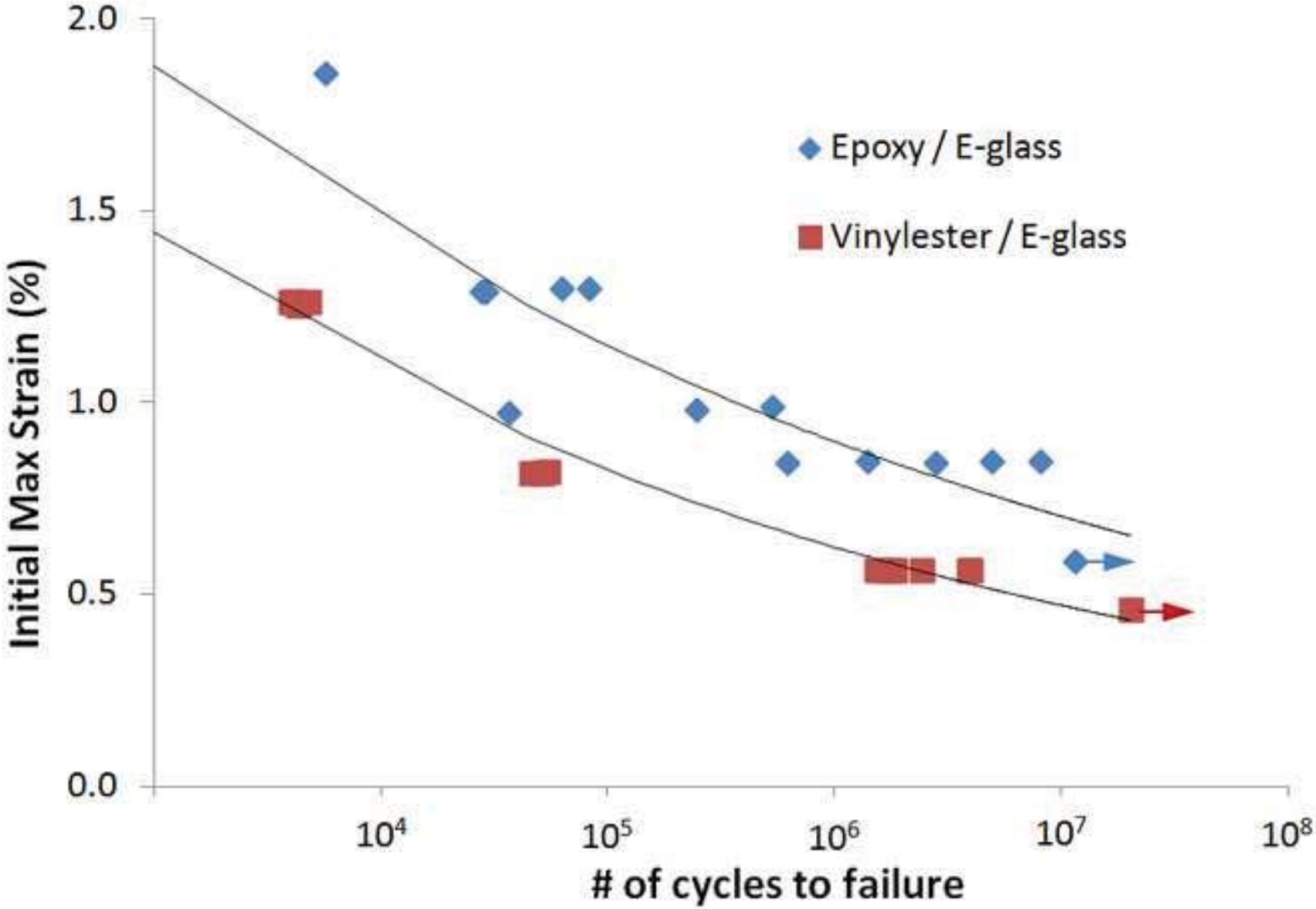

Figure 12 Test results for QI laminates ($R = 0.1$)

Figure
Click here to download high resolution image

0.81% Initial strain, R = 0.1
# of cycles to failure 52,041
(a)

0.85% Initial strain, R = 0.1
# of cycles to failure 8,130,871
(b)

Figure 13 Post fatigue-test specimens of Vinyl ester (a) and Epoxy (b)

Figure
Click here to download high resolution image

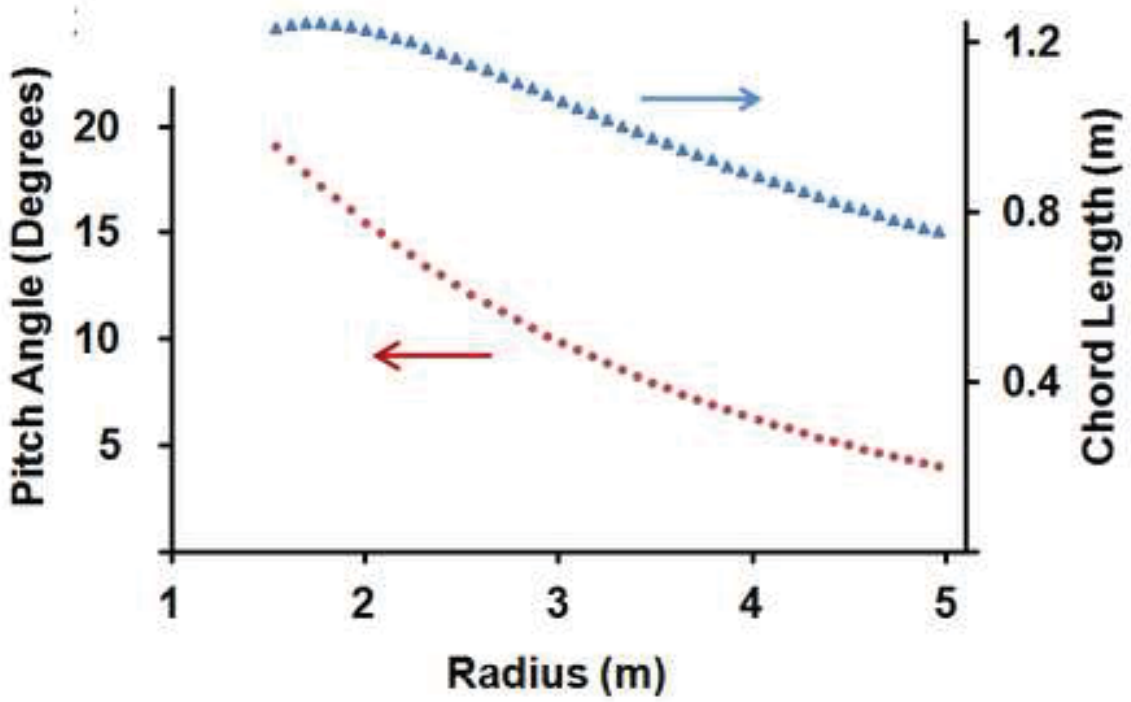

Figure 14 Radial distributions of blade pitch angle and chord length calculated using hydrodynamic model for 2.6 m/s water velocity

Figure
Click here to download high resolution image

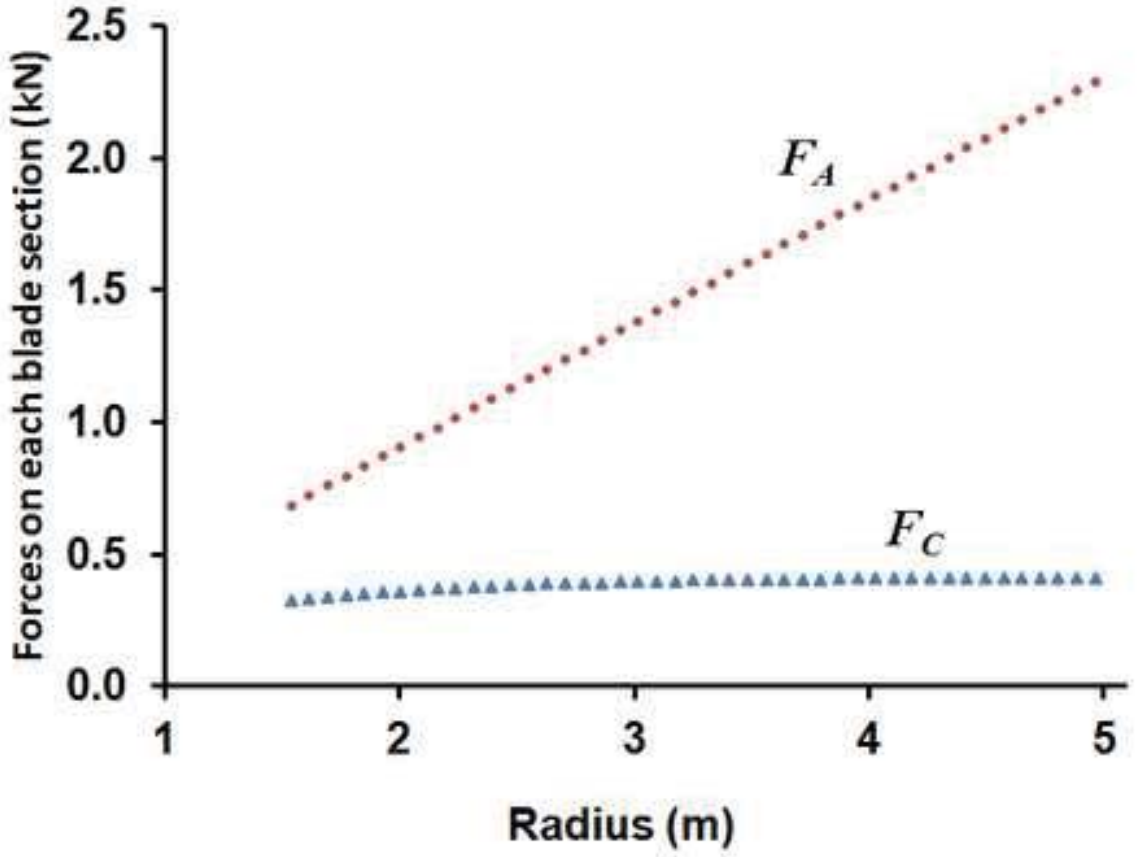

Figure 15 Radial distributions of axial (F_A) and tangential (F_C) forces from hydrodynamic model at 2.6 m/s water velocity

Figure
Click here to download high resolution image

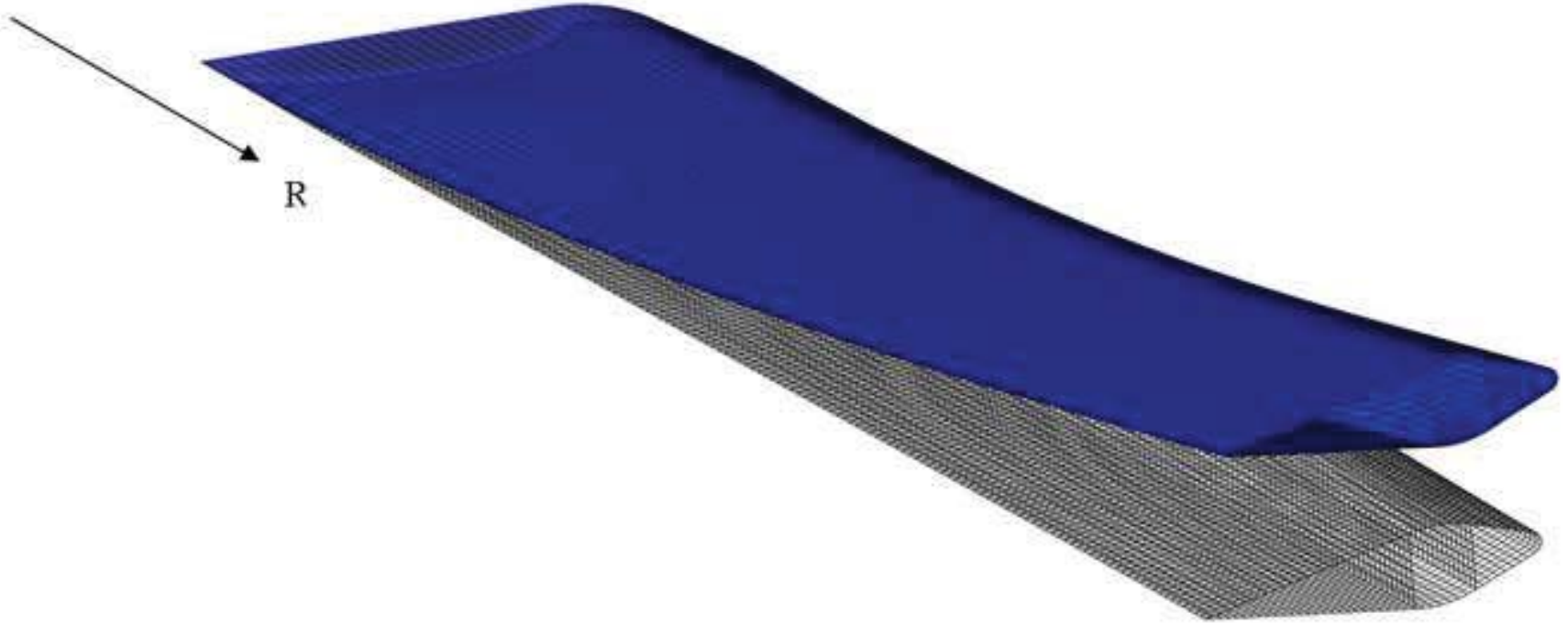

Figure 16 Undeformed and deformed shape of blade at 2.6 m/s water velocity, with a factor of safety of 2.0 applied.

Figure
Click here to download high resolution image

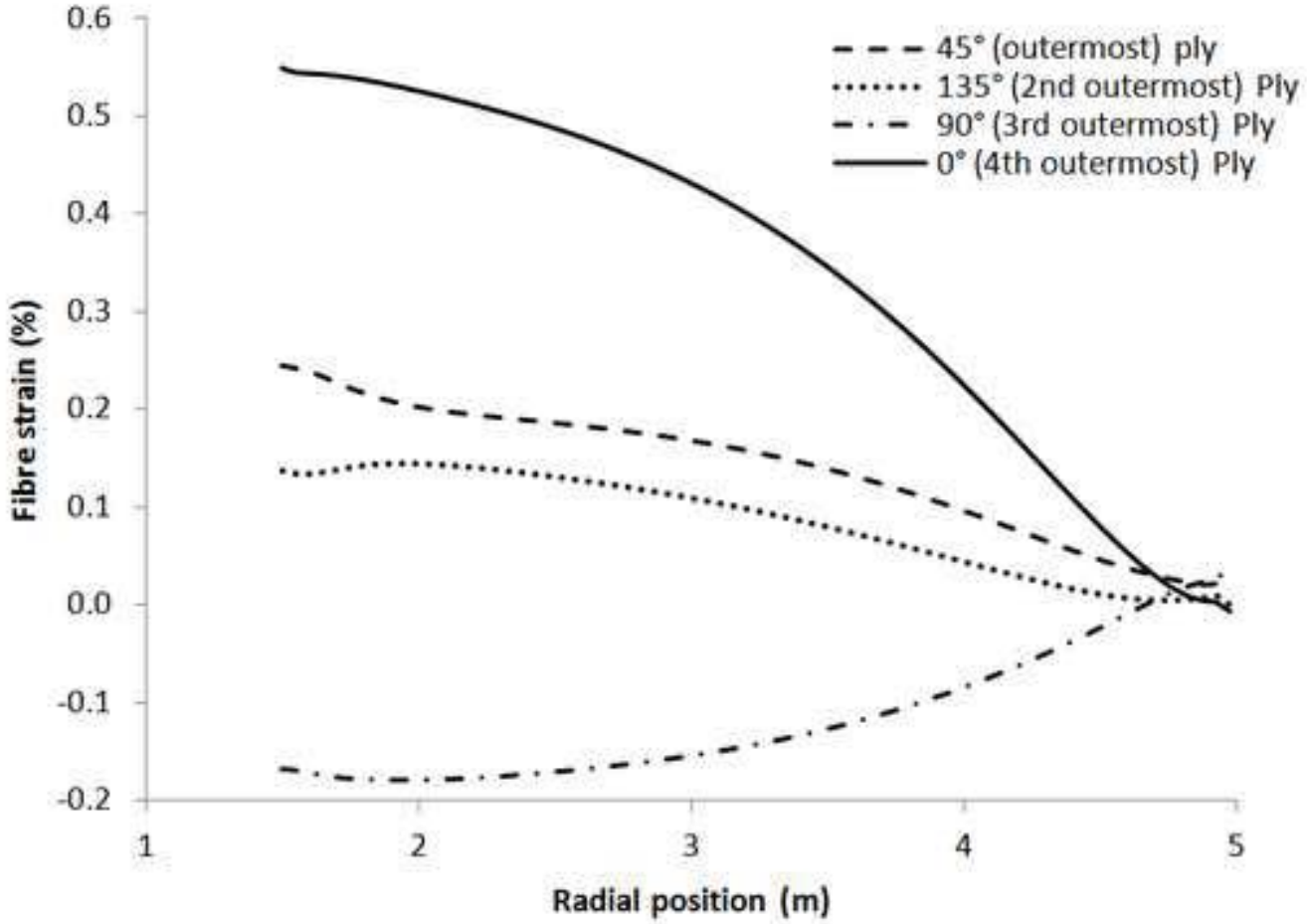

Figure 17 Fibre strains in the four outermost plies at maximum strain locations along blade operating in 2.6 m/s water velocity

Figure
Click here to download high resolution image

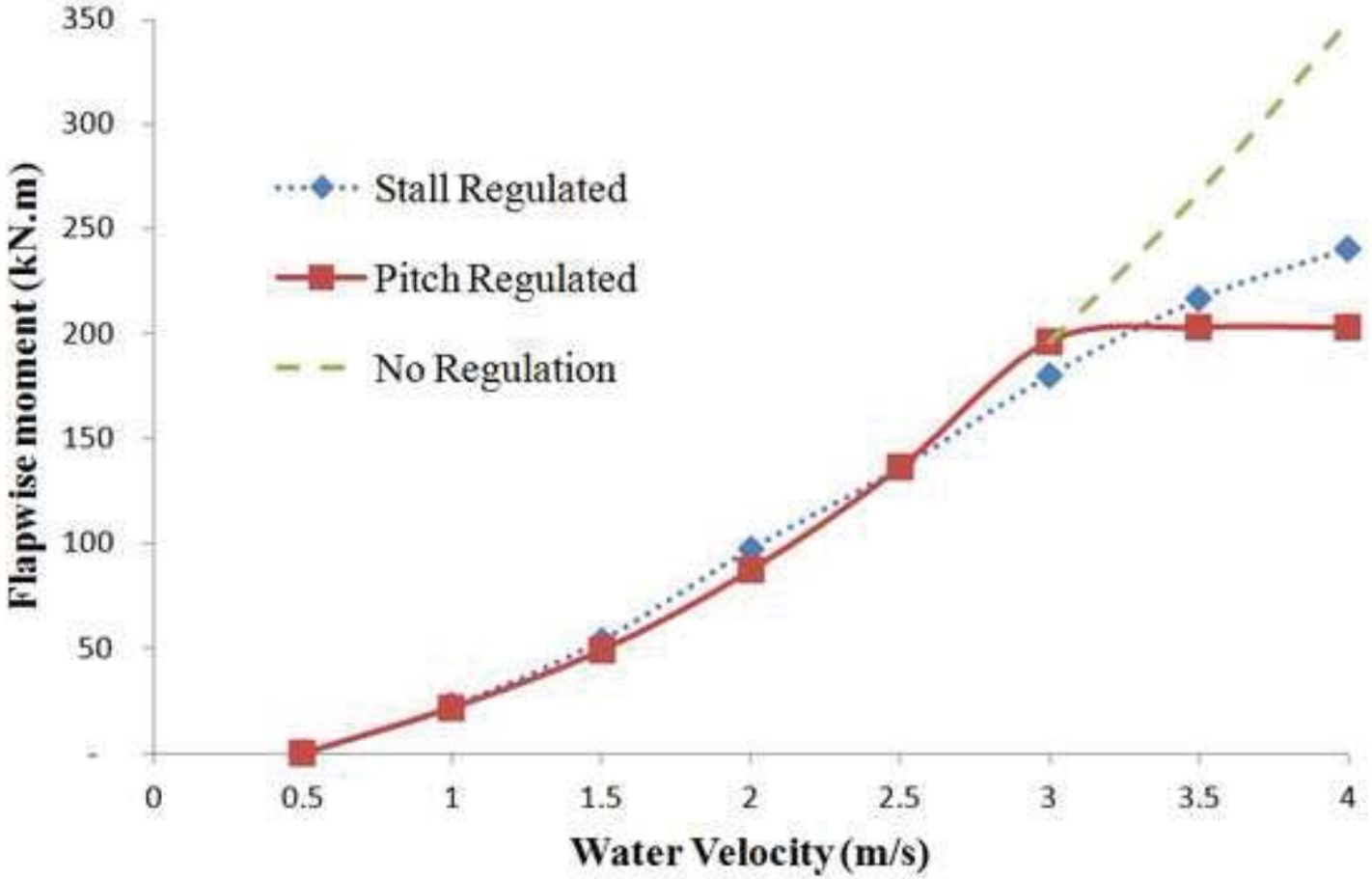

Figure 18 Predicted effect of water velocity on blade bending moment (at R = 1.5 m) for various control strategies, as calculated using hydrodynamic model

Figure
Click here to download high resolution image

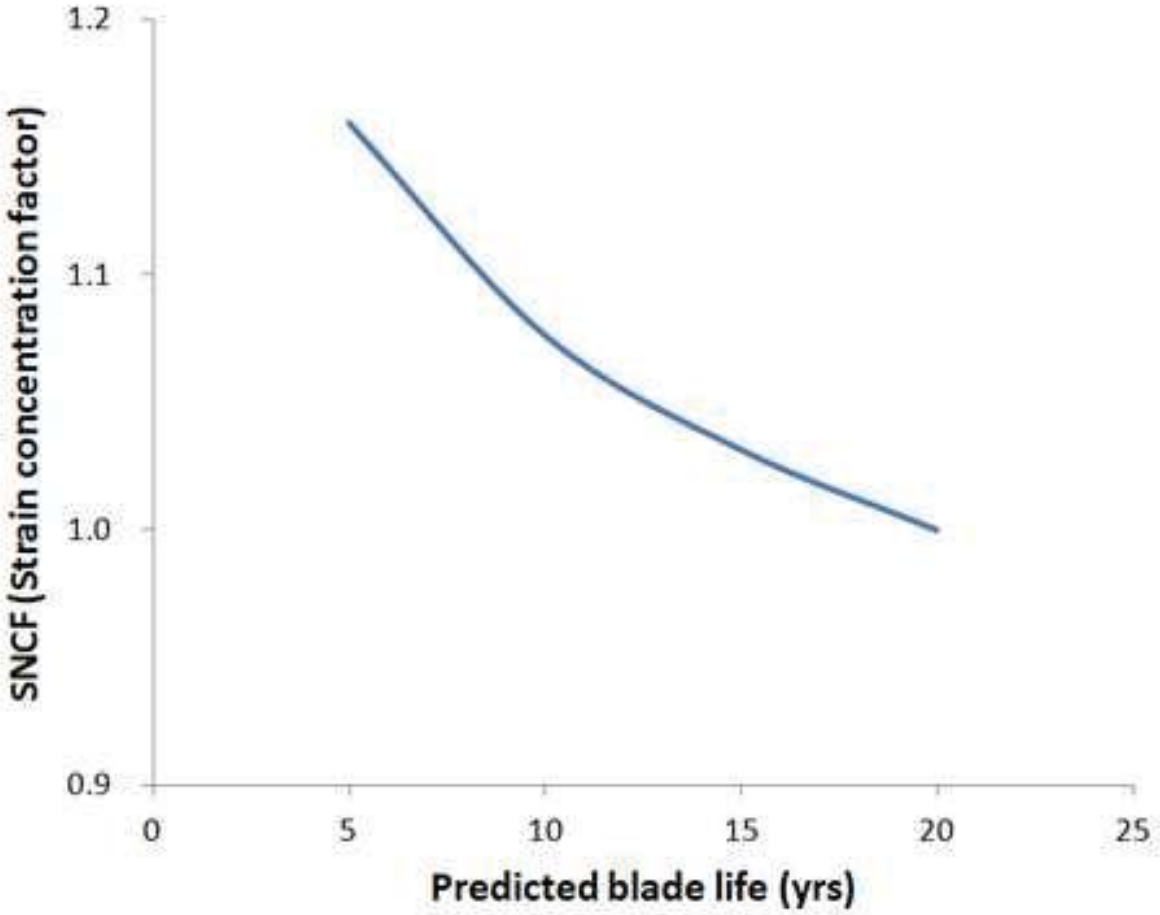

Figure 19 Predicted effect of stress concentrations on blade life for pitch regulated turbine in a tidal zone with 4.0 m/s maximum velocity and 60% neap/spring variation

Figure
Click here to download high resolution image

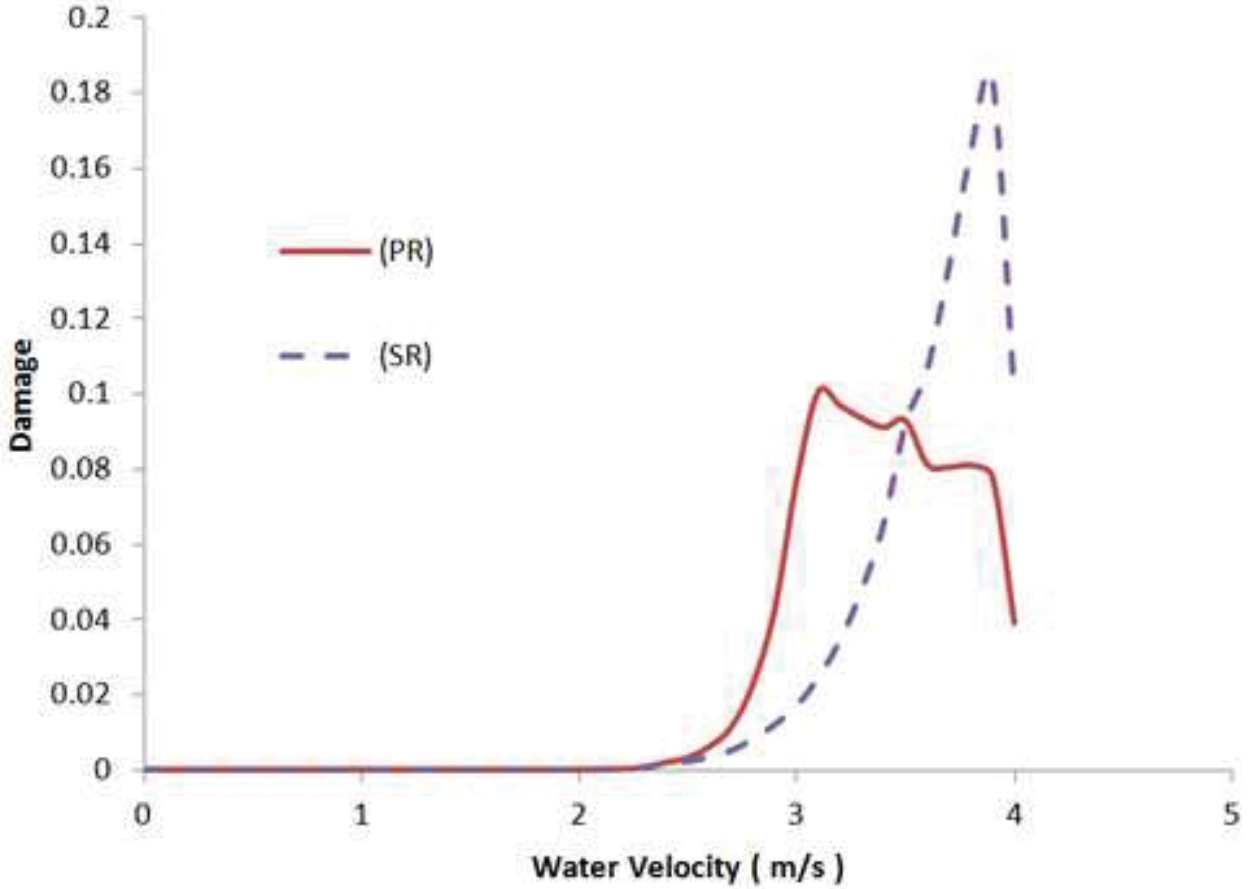

Figure 20. Damage accumulation pattern for pitch regulated (PR) and stall regulated (SR) epoxy/E-glass turbine blades running in a tidal zone with 4.0 m/s maximum velocity and 60% neap/spring variation.

Figure
Click here to download high resolution image

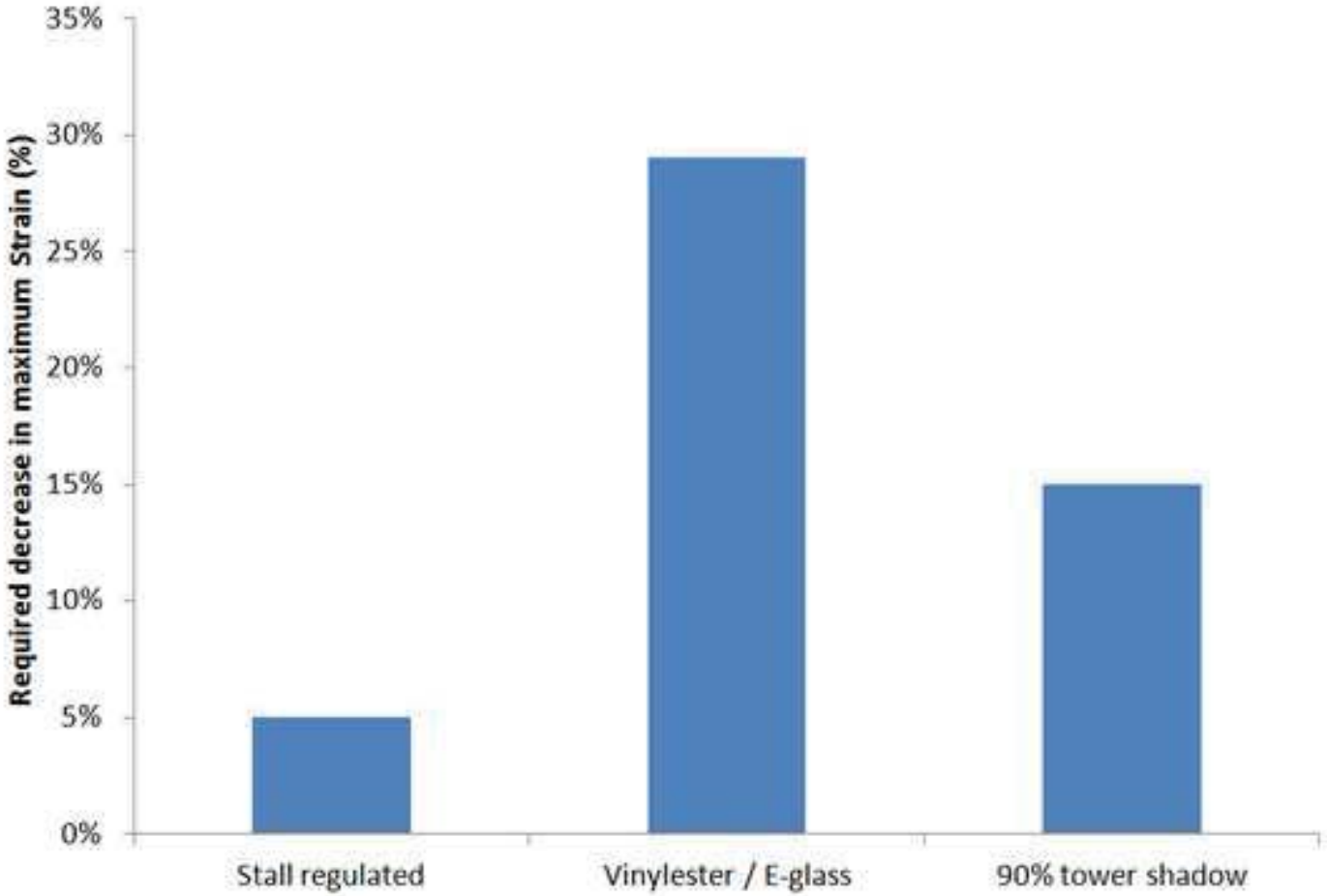

Figure 21. Comparison of required reductions in maximum strain due to various design changes, for a fatigue life equal to that of the reference case of Table 4.